Department of Physics and Astronomy

Univesity of Heidelberg

Bachelor Thesis in Physics

submitted by

Alvaro Garmendia Navarro

born in Donostia - San Sebastián (Spain)

2021

Towards re-trapping highly charged argon in a cryogenic Paul trap experiment

This Bachelor Thesis has been carried out by Alvaro Garmendia Navarro at the
Max-Planck-Institut für Kernphysik in Heidelberg
under the supervision of
apl. Prof. Dr. José R. Crespo López-Urrutia

Abstract

To enable the re-trapping of highly charged argon inside the cryogenic Paul trap as part of the Cryogenic Paul Trap Experiment-II (CryPTEx-II), part of the Max-Planck-Institut für Kernphysik, the beamline connecting a HD-compact EBIT with the cryogenic Paul trap was optimized. Argon ions are extracted from the EBIT and subsequently guided through the beamline. The charge state of the ions were identified by time of flight measurements and Ar^{13+} was selected. Near the end of the beamline, the selected ions were decelerated by a pulsed drift tube and their resulting energy was determined. Finally, they were injected into the Paul trap, whose mirror electrodes were tested for re-trapping.

Zusammenfassung

Um im Rahmen des Cryogenic Paul Trap Experiment-II (CryPTEx-II) des Max-Planck-Instituts für Kernphysik das Re-Trapping von hochgeladenem Argon innerhalb der kryogenen Paul-Falle zu ermöglichen, wurde die Beamline, die eine HD-compact EBIT mit der kryogenen Paul-Falle verbindet, optimiert. Argon-Ionen werden aus dem EBIT extrahiert und anschließend durch die Beamline geführt. Der Ladungszustand der Ionen wurde durch Flugzeitmessungen identifiziert und Ar^{13+} wurde ausgewählt. Am Ende der Beamline wurden die ausgewählten Ionen durch eine gepulste Driftröhre abgebremst und ihre resultierende Energie bestimmt. Schließlich wurden sie in die Paul-Falle injiziert, deren Spiegelelektroden auf Re-Trapping geprüft wurden.

Contents

1 Introduction **1**

1.1 Standard Model and beyond . . . 2

1.2 CryPTEx-II . . . 2

1.3 Thesis outline . . . 3

2 Theoretical background **4**

2.1 Electron beam ion trap . . . 4

2.1.1 Energy of the electron beam . . . 4

2.1.2 Electronic processes in the EBIT . . . 4

2.1.3 Evolution of the charge states . . . 7

2.1.4 Extraction from the EBIT . . . 8

2.1.5 Emittance of the ion beam . . . 9

2.2 Ion optics . . . 10

2.2.1 Proper time . . . 10

2.2.2 Geometric optics . . . 11

2.2.3 Electrostatic optics . . . 13

2.2.4 Einzel lens . . . 15

2.2.5 Deceleration of ions . . . 17

2.3 Paul Trap . . . 17

3 Experimental setup **21**

3.1 XUV EBIT . . . 23

3.1.1 Magnet assembly . . . 23

3.1.2 Drift tubes . . . 23

3.1.3 Electron gun and collector . . . 23

3.2 Beamline . . . 24

3.2.1 Sikler lens . . . 24

3.2.2 Bender . . . 25

3.2.3 Pulsed drift tube . . . 26

3.2.4 Diagnostics . . . 26

3.2.5 Timing of the beamline . . . 28

3.3 CryPTEx-II Paul trap . . . 30

4 Optimisation of the beamline **33**

4.1 XUV EBIT electrodes . . . 33

4.2 Charge state identification . . . 33

4.3 Charge state selection 34
4.4 Slow down of ions 37
4.5 Energy analysis 42
4.6 Towards re-trapping of Ar^{13+} 45

5 Conclusion and outlook **48**

"Most human beings have an almost infinite capacity for taking things for granted."

-Aldous Huxley [1]

1 Introduction

Fundamental constants have been a key part of physics since Newton introduced the gravitational constant G in his law of universal gravitation. Ever since then, many constants have been derived and were thought to be universal and everlasting, insensitive to time. But time brought countless scientists trying to resolve the unknown, discovering the mechanics behind nature itself. Newton himself started a physics revolution in the 17th century by looking at light behind a prism, revealing its composition of multiple colors and its refraction [2]. Centuries later, Joseph von Frauenhofer discovered discrete dark line in the spectrum of the sun and measured their wavelength in 1814. Only about 45 years later, Bunsen and Kirchhoff saw the same lines after heating up different elements [3], deducing that the same elements they had heated were present in the sun. These measurements were the first spectroscopies ever done and the foundation of what was to come: modern atomic physics. In 1914 Niels Bohr and Ernest Rutherford postulated their own atomic-model, which explained the spectral emission lines of hydrogen, managing to give the experimentally known Rydberg formula a theoretical support. However, this model failed to explain the existence of fine structure and hyperfine structure in spectral lines, which are now known to be caused because of relativistic and spin effects. As by many processes, so has the fine structure a constant related to it, α. Since 1970, many laws of physics have been unified under the so called Standard Model (SM), which succeeds in explaining many phenomena in the world, but fails to do so with gravity. Moreover, it is inconsistent with the Lambda-CDM model, the Standard Model of cosmology. Such flaws motivate the search for physics beyond the Standard Model (BSM) to solve its deficiencies. How this motivates the work presented in this thesis and its outline is presented in the following chapters.

1.1 Standard Model and beyond

After the experimental confirmation of quarks in the mid 1970s, the current formulation of the Standard Model was finalized. Ever since then, many experimental measurements have added further confidence in it, such as the confirmation of the top quark [4] [5], the tau neutrino [6] and most recently, the Higgs boson in 2012 [7]. Nonetheless, large scale processes, part of cosmology, cannot be precisely explained by the SM, but rather by the Lambda-CDM model. Processes that govern in the large scales have been replicated with the use of large colliders that employ huge energies, most famously the LHC at CERN which runs at energies in the TeV range. These colliders are usually the product of huge collaborations that are able to put the immense quantity of resources needed for such experiments, therefore, smaller institutions with less resources available have been focused in testing the SM with other means. Instead of looking for predicted particles at higher energies, the SM is being tested by looking at time variances of fundamental constants, such as the before mentioned fine structure constant α. This can be done with atomic clocks since they are also subject to variations of α. In the last 70 years they have been subject of many improvements, as shown in 1.

As part of the search for increased precision, atomic clocks with highly charge ions (HCI) are being built, due to their increased sensitivity to variations in α and their relative numbness to external perturbations in comparison to neutral atoms (neutrals) or lesser ionized species [8]. In that regard the Electron Beam Ion Trap (EBIT) is of huge relevancy. In 1988, the group lead by Morton Levine developed the first EBIT at the Lawrence Livermore National Laboratory [9] after further developing the Electron Beam Ion Source (EBIS) presented by E.D. Donets in Dubna, Russia [10]. The EBITs have been also improved over time, leading to the Heidelberg compact-EBIT model [11] presented by the Max Planck Institut für Kernphysik in one of their collaborations. Such an EBIT was used at the Cryogenic Paul Trap Experiment (CryPTEx), which used a quadrupole ionic trap to measure transitions.

1.2 CryPTEx-II

After the success of CryPTEx, J. Stark [13] designed the second iteration of the experiment in which a radio frequency trap consisting of a superconducting resonator would be used to trap HCIs. The ions are then cooled by sympathetic cooling via laser-cooled Be^+ ions to perform quantum logic spectroscopy on them. Firstly, the ions are produced in the XUV EBIT, a Heidelberg compact-like EBIT. Then, the ions are transported through a beamline towards the trap, in which Ar^{13+} is selected and subsequently slowed down by a serrated pulsed drift tube. The HCIs arrive at the Paul to get sympathetically cooled by

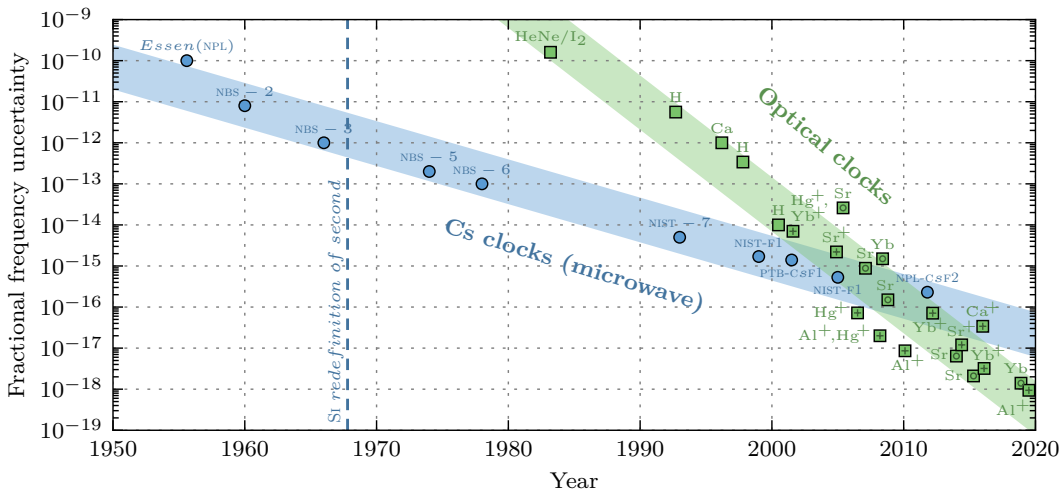

Figure 1: Improvement of the atomic clocks over time showed as their fractional frequency uncertainty. Taken from [12].

laser-cooled Be^+ ions. The produced crystal is steadily reduced until only a HCI is left, with which quantum logic spectroscopy is performed. In order to do said spectroscopy, an XUV frequency comb is produced on a different set-up built as part of the dissertation by J. Nauta [14]. For the latest state of affairs of the XUV comb, refer to [15].
However, the experiment still lives in its early stages. The XUV comb is not ready yet, since it has to be finished and moved to the surroundings of The Paul trap. Furthermore, while Be^+ ions have been already trapped, the trapping of HCIs has not been done yet, meaning that a proof of concept is still due.

1.3 Thesis outline

The goal of this work is to trap highly charged argon, specifically Ar^{13+} ions, inside the Paul trap. In order to do so, the XUV EBIT has to be set up to extract highly charged argon while using low kick voltages and the beamline needs to be tuned in for the transport of argon-like ions. Meanwhile, its 13th charge state has to selected before reaching the serrated pulsed drift tube, which slows down the ion bunch to energies below $200\,\mathrm{V} \times \mathrm{charge}$. Finally, the timing needed to close the trap after injecting the HCIs must be determined.
In Chapter 2 the theoretical background required to understand the production, transport and trapping of HCIs in this experiment is discussed. Then, in Chapter 3 the experimental setup is presented, while the optimization of the beamline and the analysis of the process is documented in Chapter 4. Lastly, the work is summarized and discussed in Chapter 5 with an outlook of the near future.

2 Theoretical background

In part 2.1 of this chapter, the relevant processes in the production and trapping of highly charged ions (HCI) in an electron beam ion trap (EBIT) will be explained. Part 2.2 addresses Ion optics and the theory behind the bunching mechanism. Lastly, 2.3 will cover the ideal Paul trap.

2.1 Electron beam ion trap

Electron beam ion traps are devices used to produce and store highly charged ions. The main tool in that process is the electron beam, which is produced by accelerating electrons from a negative biased hot cathode to an anode passing through the center of the trap, consisting of a set of electrodes. Neutral elements are then injected at the center of the trap, and the electron beam interacts with the bound electrons, resulting in their ionization or excitation. The produced ions are trapped by two potentials: in radial direction they will be attracted to the electron beam due to its space charge potential; in axial direction a static electric field is applied, so that the ions cannot leave the trapping potential. In order to extract the ions, the effective potential applied in the axial direction can be inverted.

2.1.1 Energy of the electron beam

The energy of the electron beam is of particular interest due to its relevancy in the ionization process. It depends on the cathode voltage U_{cathode} and the ones at the trap electrodes U_{trap} and is proportional to the elementary charge e. One has to also consider the emission voltage U_{emission} needed to extract the electron from the surface of the cathode, which correlates to the work function, as well as the space charge effects caused by both the ions U_{ion} and the beam U_{beam}:

$$E_{\text{beam}} = -e\,\left(U_{\text{trap}} + U_{\text{beam}} + U_{\text{ion}} - U_{\text{cathode}} - U_{\text{emission}}\right). \tag{2.1}$$

This leads to a small deviation from the simple estimation $E_{\text{beam}} = e\,(U_{\text{trap}} - U_{\text{cathode}})$.

2.1.2 Electronic processes in the EBIT

Due to the overlap between the ions and the electron beam, the ions will experience electron impact ionization, electronic excitation and electronic recombination. Additionally, ions will interact with the newly injected neutrals, leading to charge exchange between ions and neutrals.

Electron impact ionization (EII)

The most important electronic processes for this work is the ionization of an element $X^{Z_{\text{ion}}+}$ produced by the impact of a beam electron e^-_{beam}:

$$X^{Z_{\text{ion}}+} + e^-_{\text{beam}} \longrightarrow X^{(Z_{\text{ion}}+1)+} + e^-_{\text{beam}} + e^-_i, \tag{2.2}$$

where e_i describes the emitted electron and Z_i the charge number. This process can only happen if the energy of the interacting electron E_e is higher than the ionization energy of the element $X^{Z_{ion}+}$. The binding energies of the elements relevant to this work are shown in 8. The cross section of this process is described by the semi-empirical Lotz equation [16]:

$$\sigma^{\text{EII}}_{q\to q+1} = \sum_{i=1}^{N} a_i n_i \frac{\ln(E_e/E_i)}{E_e E_i} \left(1 - b_i \, exp\left[-c_i \left(\frac{E_e}{E_i} - 1\right)\right]\right). \tag{2.3}$$

Here, E_i is the ionization energy; the different i-s describe the different shells an electron can come from; n_i is the occupation number of the corresponding shell and a_i, b_i, c_i are constants that have to be determined by theory or estimated via experiments.

Electronic recombination

Electron-ion interaction between ions and electron in the trap can also end up in an ion recombinating with an electron. Due to the excess of energy $E_{\text{ex}} = E_e + E_i$, either a photon γ with energy $E_\gamma = \hbar\omega$ is emitted (radiative recombination RR) or the electron moves to an excited state if the excess energy matches an electronic transition. However, the second case only occurs at resonant energies, in which the EBIT was not operated during this work and thus it is not further discussed. The radiative recombination can be described as:

$$X^{Z_{\text{ion}}+} + e^-(E_e) \to X^{(Z_{\text{ion}}+)-1} + \gamma(E_\gamma) \quad , \quad E_\gamma = E_{\text{ex}}, \tag{2.4}$$

with E_γ being the energy of the emitted photon. The cross section of the radiative recombination is [17]:

$$\sigma^{\text{RR}}_{q\to q-1} = \frac{8\pi}{3\sqrt{3}} \alpha \, \lambda\!\!\!^{-2}_C \, \chi \ln\left(1 + \frac{\chi}{2\, n^2_{0,\text{eff}}}\right) \quad , \quad \chi = 2\, Z^2_{\text{eff}} \frac{R_y}{E_e}, \tag{2.5}$$

with the fine structure constant α, the reduced Compton wavelength $\lambda\!\!\!^{-}_C$, and the effective nuclear charge $Z_{\text{eff}} = (Z + q)/2$. The effective principal quantum number $n_{0,\text{eff}} = n_0 + (1 - \omega_0) - 0.3$ takes into account the principal quantum number n_0 and the ratio ω_0 between occupied and not occupied states in the n_0 shell.

Electron impact excitation EIE

An electron may also have an effect on an ion without being captured by it. In this case, the electron collides with a bound electron. transferring energy to it and thus exciting it:

$$X^{Z_{\text{ion}}+} \; + \; e^-(E_e) \rightarrow \left[X^{Z_{\text{ion}}+}\right]^* \; + \; e^-\left(E_e'\right) \;\; , \; E_e < E_e', \tag{2.6}$$

where * stands for excited and E_e' is the energy f the colliding electron after the impact. The cross section of the electron impact excitation depends on both the electron Energy E_e and the structure of the of the targeted ion and can be approximated by the empiric equation by van Regemorter [18]:

$$\sigma_{q\rightarrow q}^{\text{EIE}} \approx \frac{8\pi^2}{\sqrt{3}} a_0^2 f_{ij} \frac{R_y^2}{E_{ij}^2} \frac{G(x)}{x} \;\; \text{, with } \; x = \frac{E_e}{E_{ij}}. \tag{2.7}$$

a_0 denotes the Bohr radius, $R_y = 13.6\text{eV}$ is the Rydberg energy and f_{ij} describes the strength of the oscillation between the implicated levels in the targeted ion. $G(x)$ is the effective Gaunt factor and per [18] can be approximated to:

$$G(x) = 0.349 \ln x + 0.0988 + 0.4555 x^{-1}. \tag{2.8}$$

Charge exchange CX

Due to the presence of lesser ionized elements and neutrals (Y in the following equation), electrons of the HCI may transfer to lesser energetic states of the lesser ionized species emitting a photon in the process:

$$X^{Z_{\text{ion}}+} \; + Y \rightarrow X^{(Z_{\text{ion}}+)-1} \; + Y^+ \; + \gamma(E_\gamma) \;\; , \text{ with } \;\; E_\gamma = E_{i,X^{(z_{\text{ion}}+)-1}} - E_{i,Y}, \tag{2.9}$$

where $E_{i,(X,Y)}$ is the ionization energy of the corresponding ion. Either ion may end up in an excited state, in which case the photon Energy E_γ would be lowered by the corresponding excitation energy. The cross section of the charge exchange is described by [19]:

$$\sigma_{q\rightarrow q-1}^{\text{CX}} = \pi a_0^2 q^2 \frac{R_y^2}{E_{i,Y}}. \tag{2.10}$$

Relaxation-Recombination

Several of the before-mentioned processes produce excited ions. There are two ways in which such an ion can relax itself: radiation of a photon or an electron. The first process follows the form:

$$\left[X^{Z_{\text{ion}+}}\right]^* \rightarrow X^{Z_{\text{ion}+}} + \gamma\left(E_\gamma\right) \quad , \quad \Delta E_\gamma = \left[X^{Z_{\text{ion}+}}\right]^* - X^{Z_{\text{ion}+}}. \tag{2.11}$$

The second process, radiation of an electron, is also called auto-ionization or auger decay. It follows the form:

$$\left[X^{Z_{\text{ion}+}}\right]^* \rightarrow X^{Z_{\text{ion}+}} + e^-\left(E_e\right) \quad , \quad \Delta E_e = \left[X^{Z_{\text{ion}+}}\right]^* - X^{Z_{\text{ion}+}}. \tag{2.12}$$

2.1.3 Evolution of the charge states

The charge state distribution of the HCIs inside an EBIT are not stationary and evolve over time. In order to describe this evolution one has to take into account the rates with which the before-mentioned processes happen. In addition to that, the flux of injected neutrals (IN) and the escape rate of the ions (ESC) has to be taken into account too:

$$n_q = R^{\text{EII}}_{q-1\rightarrow q} - R^{\text{EII}}_{q\rightarrow q+1} + R^{\text{RR}}_{q-1\rightarrow q} - R^{\text{RR}}_{q+1\rightarrow q} + R^{\text{CX}}_{q\rightarrow q-1} - R^{\text{CX}}_{q+1\rightarrow q} + R^{\text{IN}} - R^{\text{ESC}}, \tag{2.13}$$

with n_q being the density of ions populating the charged state q and R^i the rate of each process. The different rates are given by:

$$R^{\text{EII}}_{q\rightarrow q+1} = \frac{J_e}{e} n_q \sigma^{\text{EII}}_{q\rightarrow q+1} f_{e,i}, \tag{2.14}$$

$$R^{\text{RR}}_{q\rightarrow q-1} = \frac{J_e}{e} n_q \sigma^{\text{RR}}_{q\rightarrow q-1} f_{e,i}, \tag{2.15}$$

$$R^{\text{CX}}_{q\rightarrow q-1} = n_0\left(p_{\text{IN}}\right) n_q \sigma^{\text{CX}}_{q\rightarrow q-1} \bar{v_q}, \tag{2.16}$$

with J_e the density of the electron beam, e the electron charge, $f_{e,i}$ a factor that takes into account the overlap between ion cloud and electron beam and n_0 the neutral gas density that depends on the injection pressure p_{IN}. The different σ^i refer to the ones described in equations 2.3, 2.5, 2.10. $\bar{v_q}$ is the mean velocity of the ions, which can be calculated by:

$$\bar{v_q} = \sqrt{\frac{8 k_b T_{\text{ion}}}{m_{\text{ion}} \pi}}. \tag{2.17}$$

This calculation applies under the assumption of a thermal equilibrium, at which the velocity would follow a Maxwell-Boltzmann distribution, which is not given in an EBIT, but is used

here as an approximation. The rate R^{IN} comes from the injection of neutrals that are ionized through electron impacts. This term is thus only relevant for the first ionization state:

$$R^{\mathrm{IN}} = \frac{J_e}{e} n_0 \sigma^{\mathrm{EII}}_{q=0\to q=1} \;\text{ for }\; q=1 \;\;;\; R^{\mathrm{IN}} = 0 \;\; \forall \;\; q>1. \tag{2.18}$$

Lastly, the escape rate R^{ESC} is made up of the leaking ions in axial and radial direction. It is given by [20]:

$$R^{\mathrm{ESC}}_q = n_q \nu_q \left(\frac{\exp -\omega_q}{w_q} - \sqrt{\omega_q}\left[\mathrm{erf}(\omega_q) - 1\right] \right), \tag{2.19}$$

with:

$$w_q = \frac{eqV}{k_B T_{ion}}, \tag{2.20}$$

$$\mathrm{erf}(z) = \frac{2}{\sqrt{\pi}} \int_0^z e^{-\tau^2} \mathrm{d}\tau. \tag{2.21}$$

In which V is the trapping potential and nu_q is the Coulomb collision rate of ions with charge q.

2.1.4 Extraction from the EBIT

In order to extract ions from an EBIT, the trapping potential ϕ_{trap} is lifted, so that the ions have enough energy to fly through the end cap potential ϕ_{ec} and escape. The potential to which the trap is risen is called the kick potential ϕ_{kick} and it is the biggest contributor to the energy of the ions when they leave the trap since the beamline only presents conservative potentials (with the exceptions of the pulsed drift tubes, see chapter 3.2.3). The other two factors that have to be taken into account are the space charge effects ϕ_{SC} and the thermal distribution of the ions E_{T}. The energy of an ion with given charge state q is thus

$$E_{\mathrm{ion}} = qe(\kappa\phi_{\mathrm{kick}} + \phi_{\mathrm{SC}}) + E_{\mathrm{T}}, \tag{2.22}$$

where $1 \geq \kappa \geq \phi_{\mathrm{ec}}/\phi_{\mathrm{kick}}$ accounts for the fact that ions may leave the trap before the kick potential Φ_{kick} is reached but after the end cap potential ϕ_{ec} is surpassed.

The space charge effects of the electrons are higher than the ones induced by the ions themselves, therefore the energy of the ion cloud is decreased by these effects. $\vec{E}_{\mathrm{T}} \approx 0$ can be approximated for the ion cloud in addition to $\kappa \approx 1$ due to the low kick voltage used in this work which leads to the energy approximation:

$$E_{\mathrm{ion}} \approx qe\phi_{\mathrm{kick}} \;\text{ with }\; \Delta E_{\mathrm{ion}} \approx \Delta E_{\mathrm{T}}. \tag{2.23}$$

Taking into account that this ion energy is equivalent to the kinetic energy, the velocity of an ion is estimated as:

$$v_{\mathrm{ion}} = \sqrt{\frac{2E_{\mathrm{ion}}}{m}} = \sqrt{\frac{2qe\kappa\phi_{\mathrm{kick}}}{m}}. \tag{2.24}$$

2.1.5 Emittance of the ion beam

After the extraction, the ion beam also possesses a radial component that has to be accounted for. Introducing the emittance [21], [22]; this characteristic can be quantified. It describes the area of the ion beam in phase space and the fraction that can be accepted by a beamline

$$\epsilon = \sigma_r \sqrt{\frac{k_B T}{2qe\Phi_{\text{kick}}}}, \tag{2.25}$$

where σ_r is the average radial spread of the beam and k_B the Boltzmann-constant. Comparing with Equation 2.22, this simplifies to

$$\epsilon_r = \sigma_r \sqrt{\frac{E_{\text{T}}}{2E_{\text{ion}}}}. \tag{2.26}$$

The emittance of the ion beam is thus proportional to $1/v_{\text{ion}}^2$, meaning that the acceptance of the beamline is lower for slow ion beams. Besides, the radial emittance cannot be controlled with the beamline due to the low effect of the optical elements in the thermal energy of the ions.

2.2 Ion optics

In this chapter the basics behind ion optics will be discussed regarding the characteristics of the time of flight of an ion, an introduction into optics and electrostatic optics following to the einzel lens and the how the deceleration of ions can be achieved. Due to the "slow" velocities present at the experiment, the following calculations will be carried out at non-relativistic velocities $\vec{v}$. Besides, all the optical elements used in the beamline use electrostatic potentials, so the author will focus only on this scenario.

2.2.1 Proper time

An ion flying through an electrostatic potential Φ experiences a force $\vec{F}$ that alters it trajectory and its velocity:

$$\vec{F} = qe\vec{E} = qe\vec{\nabla}\Phi. \tag{2.27}$$

Where q is the charge state of the ion (e.g. 13 for Ar^{13+}) and e is the electron charge. By using equation 2.24 for the velocity and $\vec{a} = \vec{F}/m$ for the acceleration, the equation of motion follows

$$\vec{r}(t) = \frac{\vec{a}}{2}t^2 + \vec{v_0}t + \vec{r_0} = \frac{\vec{\nabla}\Phi}{2}\frac{qe}{m}t^2 + \sqrt{2\kappa\phi_{\text{kick}}}\sqrt{\frac{qe}{m}}t\vec{e_z} + \vec{r_0}, \tag{2.28}$$

where $\vec{e_z}$ denotes the direction of the beam axis. For clarity, one can also define a parameter $\tau = t\sqrt{\frac{qe}{m}}$ so that the equation simplifies to

$$\vec{r}(\tau) = \frac{\vec{\nabla}\Phi}{2}\tau^2 + \sqrt{2\kappa\phi_{\text{kick}}}\tau + \vec{r_0}, \tag{2.29}$$

The parameter τ serves as a proper time for each ion type. This shows that the trajectory of the ions is independent of the ratio $\frac{qe}{m}$ and that only their time of flight varies between different charge states or masses. Furthermore, one can compare the parameter τ of two ion species and see that:

$$\sqrt{\frac{q_a e}{m_a}}t_a = \tau_a = \tau_b = \sqrt{\frac{q_b e}{m_b}}t_b, \tag{2.30}$$

following:

$$t_a = \sqrt{\frac{q_b m_a}{m_b q_a}}t_b. \tag{2.31}$$

Neglecting the difference in mass between charge states due to $m_{\text{ion}} \gg m_{\text{e}^-}$, one can infer the times of flight t_q from the time of flight of another charge state t'_q:

$$t_q = \frac{t_{q'}}{\sqrt{\Delta q}}. \tag{2.32}$$

This means that the time of flight of an ion with given charge states can be calculated as a function of the time of flight of a known one. By doing so, the charge state of a flying ion

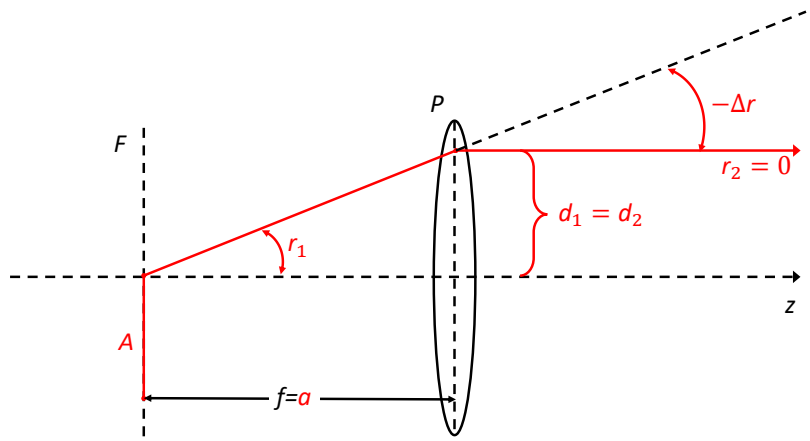

Figure 2: Schematic of a ray, which come from the focal length of the lens, being deflected.

bunch can be determined by comparing the different measured times of flight. Moreover, Equation 2.31 can also be used to compare the time of flight of a known particle, i.e. a proton, with the one of an unknown charge state to help with the identification.

2.2.2 Geometric optics

Due to the emittance of the ion beam (see chapter 2.1.5), it is of utter significance to refocus the beam on several occasions to maximize the efficiency of the transport. The einzel lens ("einzel" means "single") is an electrostatic lens that focuses the ion beam without changing its energy. The following explanation is based on [23] and will draw a comparison between light optics and electrostatic optics. Starting with basic optics, a lens is an element which imparts a deflection Δr to an incoming ray (in our case an ion beam). The deflection is proportional to the separation to the axis, at which the beams passes, but is independent of the entrance slope r_1. If the lens is thin enough, the deflection happens, approximately, on a single plane P and both the entrance and exit distances $d_{1,2}$ are the same,

$$d_1 = d_2, \tag{2.33}$$

but the slope changes upon passing through the lens

$$r_2 = r_1 + \Delta r. \tag{2.34}$$

Δr can be described by defining a proportionality constant c so that $\Delta r = -cd_1$ and can be calculated by examining the case in which the ray leaves parallel to the axis:

$$r_2 = 0, r_1 = -\Delta r = cd_1, \tag{2.35}$$

$$c = \frac{-\Delta r}{r_1} = \frac{1}{f_1}. \tag{2.36}$$

Here f_1 denotes the distance at which the ray crosses the lense and is called the focal length of the lens. Introducing the focal length in Equation 2.34,

$$r_2 = r_1 - \frac{d_1}{f_1}. \tag{2.37}$$

Furthermore, the equation can also be written in matrix form

$$\begin{pmatrix} d \\ r \end{pmatrix}_2 = \begin{pmatrix} 1 & 0 \\ -\frac{1}{f_1} & 1 \end{pmatrix} \begin{pmatrix} d \\ r \end{pmatrix}_1 = M_L \begin{pmatrix} d \\ r \end{pmatrix}_1, \tag{2.38}$$

where M_L is the so called transfer matrix of the lens with coefficients

$$a_{11} = 1, a_{12} = 0, a_{21} = \frac{-1}{f_1}, a_{22} = 1. \tag{2.39}$$

The former case can also be described by looking at the exit equation of the ray in the $z-r$ system:

$$r = ar_1 + zr_2 = ar_1 + z\left(r_1 - \frac{d_1}{f_1}\right) \tag{2.40}$$

where a describes the separation between the object A and the plane P. It is worth noting that if the energy of the ray before and past the lens is the same, the focal lengths on both sides are the same $f_1 = f_2 = f$.

Since the deflection of the ray in an einzel lens does not happen in a single, an additional transfer matrix has to be introduced. This second matrix accounts for the deflection that occurs in the lens:

$$\begin{pmatrix} d \\ r \end{pmatrix}_2 = \begin{pmatrix} 1 & L \\ 0 & 1 \end{pmatrix} \begin{pmatrix} d \\ r \end{pmatrix}_1 = M_D \begin{pmatrix} d \\ r \end{pmatrix}_1. \tag{2.41}$$

Whenever more than one optical element is put in place, the transfer matrices have to be multiplied in order to calculate the trajectory of the incoming ray:

$$\begin{pmatrix} d \\ r \end{pmatrix}_3 = \begin{pmatrix} b_{11} & b_{12} \\ b_{21} & b_{22} \end{pmatrix} \begin{pmatrix} d \\ r \end{pmatrix}_2 = \begin{pmatrix} b_{11} & b_{12} \\ b_{21} & b_{22} \end{pmatrix} \begin{pmatrix} a_{11} & a_{12} \\ {}_{21} & a_{22} \end{pmatrix} \begin{pmatrix} d \\ r \end{pmatrix}_1, \tag{2.42}$$

with b_i denoting the coefficients of the matrix M_D.

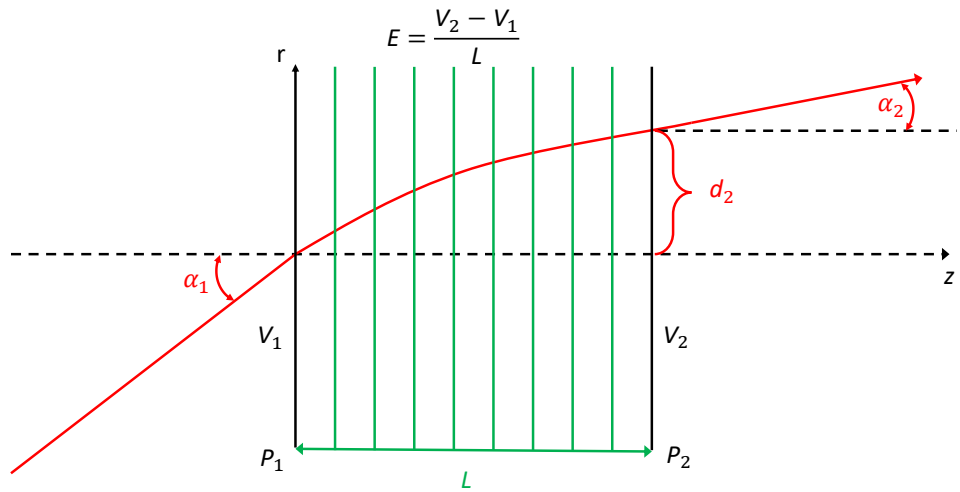

Figure 3: Deflection of a charge particle by a uniform electrostatic field. Note that α_i corresponds to the before-mentioned r_i and that r_2 corresponds to the former d_2.

2.2.3 Electrostatic optics

An electrostatic lens, such as the einzel lens, draws many similarities with an optical lens. Firstly, the deflection that occurs inside the lens, described by M_D in Equation 2.41, is similar to the passage of a charged particle through a uniform electrostatic field (see Figure 3). By defining the voltages so that the zero lies at T/q with T being the kinetic energy and q the charge of the particle, the energy of the particle inside a potential V is qV. With this definition, the motion of the particle can be calculated in the $z - r$ coordinate system:

$$\dot{z} = q\frac{E}{m}t + v_1 \cos\alpha_1, \quad z = \frac{qE}{2m}t^2 + v_1 \cos\alpha_1 t, \tag{2.43}$$

$$\dot{r} = \dot{r_1} = v_1 \sin\alpha_1, \quad r = v_1 \sin\alpha_1 t. \tag{2.44}$$

Here t is the time, m is the mass of the particle and v_1 is the velocity of the particle when entering the potential V_1 and follows $qV_1 = mv_1^2/2$. The angle α_1 is shown in Figure 3. As in chapter 2.2.1, it is of further interest to eliminate the time t from the equations to describe the trajectory:

$$t = \frac{mv_1}{qE}\left(\sqrt{\cos^2\alpha_1 + \frac{2qE}{mv_1^2}z} - \cos\alpha_1\right), \tag{2.45}$$

$$r = \frac{2V_1}{E}\sin\alpha_1\left(\sqrt{\frac{E}{V_1}z + \cos^2\alpha_1} - \cos\alpha_1\right). \tag{2.46}$$

At the exit of the electric field at $z = L$, the distance from the z-axis can be obtained with:

$$\frac{E}{V_1} = \frac{1}{L}\left(\frac{V_2}{V_1} - 1\right), \tag{2.47}$$

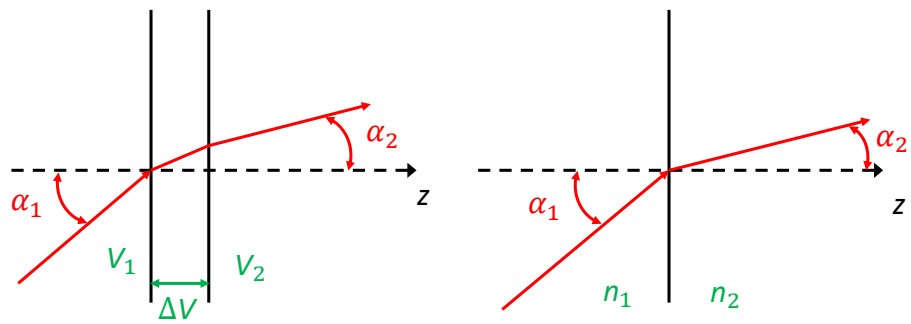

Figure 4: Refraction of a charged particle by an electrostatic lens (a) compared to that of light on a medium.

$$r_2 = \frac{2L\sin\alpha_1}{V_2/V_1 - 1}\left(\sqrt{\frac{V_2}{V_1} - \sin^2\alpha_1} - \cos\alpha_1\right). \tag{2.48}$$

Differentiating Equation 2.46 at $z + L$ lead to:

$$\dot{r_2} = \sin\alpha_1\left(\frac{V_2}{V_1} - \sin^2\alpha_1\right). \tag{2.49}$$

Now, after realizing that $\dot{r_2} = \tan\alpha_2$ and comparing with Equation 2.49:

$$\tan\alpha_2 = \frac{\sin\alpha_2}{\sqrt{1 - \sin^2\alpha_2}}, \tag{2.50}$$

$$\frac{\sin\alpha_2}{\sqrt{1 - \sin^2\alpha_2}} = \frac{\sin\alpha_2}{\sqrt{\frac{V_2}{V_1} - \sin^2\alpha_1}}, \tag{2.51}$$

from which finally follows:

$$\frac{\sin\alpha_2}{\sin\alpha_1} = \sqrt{\frac{V_1}{V_2}}. \tag{2.52}$$

An important note that shall be made is the absence of L in Equation 2.52. If the electric field could be compressed to a doubled layered surface with the potential V_1 and V_2 on each side, the deflection by an electrostatic lens would correspond to the refraction of light with $\sqrt{V_i}$ acting as the refractive indexes n_i. The main difference is that for light the transition between mediums is sharp and occurs immediately, while for a charged particle in an electrostatic lens this occurs gradually.

This explanation is valid for both accelerating and decelerating potentials. However, in case the potential is a decelerating one, its strength should be less than mv^2/mq, otherwise the charged particle would be reflected.

The presented equations can also be written in matrix form as with the optical lens, but for

sake of simplicity, the angle of incidence will be restricted to $\alpha_1 \ll 1$, following to $\sin\alpha_1 \approx \dot{r_1}$, $\cos\alpha_1 \approx 1$ and $\dot{r_1} \ll V_2/V_1$. Applying these approximation leads to:

$$r_2 \approx \frac{2L}{\sqrt{V_2/V_1 + 1}\dot{r_1}}. \tag{2.53}$$

If $r_1 \neq 0$

$$\dot{r_2} = \sqrt{\frac{V1}{V2}}\dot{r_1}. \tag{2.54}$$

This results in the matrix form

$$\begin{pmatrix} r \\ \dot{r} \end{pmatrix}_2 = \begin{pmatrix} 1 & \frac{2L}{\sqrt{V_1/V_2+1}} \\ 0 & \sqrt{V1/V2} \end{pmatrix} \begin{pmatrix} r & \dot{r} \end{pmatrix}_1 = M_F \begin{pmatrix} r \\ \dot{r} \end{pmatrix}_1 . \tag{2.55}$$

This is only valid for both acceleration and deceleration potentials.

2.2.4 Einzel lens

The einzel lens is an electrostatic lens that focuses a charged beam without changing its energy. It typically consists of three electrodes, from which the first and third one are set at the same potential V_B which can also be ground potential. The potential in the middle electrode V_em can be set either positive or negative, producing two different modes inside the lens: accel-decel and decel-accel. If the set potential is negative (accel-decel), the ion beam is focused in the outer sector and de-focused in the inside one, while accelerating the beam upon entrance and decelerating it to its original velocity once it leaves the lens. On the other side, a positive potential (decel-accel) achieves the opposite effect, a focus of the beam in the inside sector and a de-focus on the outer sector while first decelerating and the returning to the original velocity.

Both modes end up achieving a focus of the ion beam, since it travels slower on the focusing sector, however, the decel-accel mode achieves higher refractive power. In Figure 5 a simulation of an ion beam passing through an einzel lens is shown, demonstrating the higher refractive power achieved by setting a positive voltage in the middle of the lens [22]. In both cases the beam comes with the same kinetic energy $E = qeV_B$, with V_B as the accelerating voltage and qe as the charge state and the elementary charge respectively. Even though V_{em} was set to a smaller absolute value in the upper case, the refractive power is still higher than in the lower one. The advantage to setting $V_{em} > 0$ is the weaker aberration caused due to the lower distance to the optical axis r_a,

$$d_S = \frac{K_S r_a^3}{D^2}. \tag{2.56}$$

Here d_S is the diameter of the circle where the beam is focused with D as a scale factor dependent on the axial extension of the field of the lens and K_S a dimensionless lens-

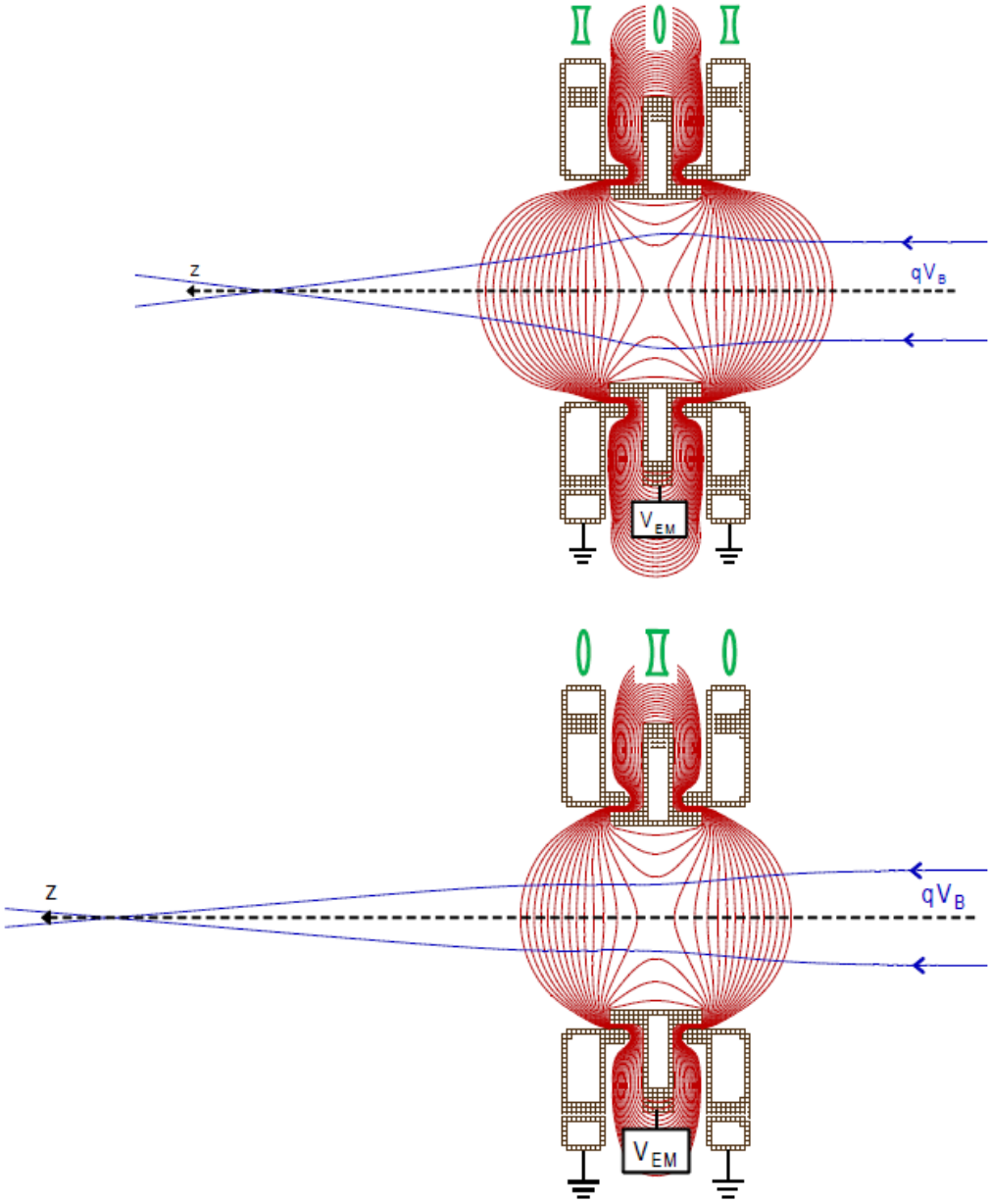

Figure 5: Simulation of the trajectory of an ion beam through an einzel lens done by L. Schmöger [22] with SIMION. The upper diagram corresponds to a lens in decel-accel mode while the lower one to a accel-decel mode.

specific factor between 2 and 10. This aberration is caused because the refractive power is not exactly proportional to the distance to the optical axis r_a, causing a focus-circle instead of a focus-point.

2.2.5 Deceleration of ions

In order to re-trap ions in the Paul trap it is necessary that they come in with low energies. To do so, at the end of the beamline a deceleration mechanism is set up.
This mechanism uses an electrodynamic potential which increases approximately linearly in the axial direction. This can be described by:

$$\Phi(t,z) = \Theta(t_s - t)\left[\Phi_{\text{low}} + \Phi_{\text{diff}}\frac{z - z_0}{d_z}\right], \tag{2.57}$$

where Θ is the heavy-side step function, t_s the switching time, Φ_{low} as the lower charged pulsed drift tube, Φ_{diff} the difference in charge between both drift tubes so that $\Phi_{\text{low}}+\Phi_{\text{diff}} = \Phi_{\text{high}}$, z_0 the start-point of the first PDT and d_z the distance between them. The shape of the potential is simulated in Figure 14. By adjusting t_s so that the potential falls down to zero when the ions reach the higher end of the potential, they end up losing energy according to:

$$\Delta E(z) = qe\Phi(t', z) = qe\left[\Phi_{\text{low}} + \Phi_{\text{diff}}\frac{z - z_0}{d_z}\right] \tag{2.58}$$

Nonetheless, the ions in the cloud have an energy distribution and will not be at the same place when the PDTs are turned off. Taking into account that all the potentials in front of the PDTs are conservative (hence no acceleration nor deceleration during the flight) and the energy distribution δE_{ion} from Equation 2.23, the location of the ions at the time t_s is:

$$z(t_s) = v_{\text{ion}}t_s = \left[\sqrt{\frac{2E_{\text{ion}}}{m}} \pm \sqrt{\frac{2\delta E_{\text{ion}}}{m}}\right] t_s. \tag{2.59}$$

Since the second term in Equation 2.58 is proportional to z, ions with higher velocity and thus higher kinetic energy, lose more energy due to the PDTs while the opposite applies for the slower ones as well. In order to optimize the braking of the ions the potential of the PDTs, particularly Φ_{diff} can be tuned as well as the trajectory leading into the drift tubes.

2.3 Paul Trap

At the end of the beamline, the CryPTEx-II Paul trap (from now on "the Paul trap") is attached to trap and store the HCIs. This chapter will briefly explain the basics of the Paul trap and how it traps ions based on [13]. In order to trap ions, the Paul trap uses a radio frequency quadrupole field (RF) produced by four hyperbolic electrodes as well as an electrostatic quadrupole field (DC). The general form of a quadrupole potential (QP) is:

$$\Phi_{\text{QP}}(x,y,z) = \left(ax^2 + by^2 + cz^2\right). \tag{2.60}$$

The parameters a, b, c follow $a + b + c = 0$ because of the Laplace equation $\Delta\Phi = 0$. It leads to $c = 0$ and $a = -b$ for a two dimensional quadrupole field in $x - y$ direction. Since a potential of this form is only capable of trapping ions in one direction, an oscillating potential is needed in order to trap in two directions:

$$\Phi_{\mathrm{RF}}(x, y, z) = \Phi_0(t) \frac{x^2 - y^2}{r_0^2}, \tag{2.61}$$

where r_0 denotes the distance between an electrode and the trap center (see Figure 6). The time-dependent quadrupole amplitude $\Phi_0(t)$ depends on the applied voltage V_0 and the trap frequency Ω:

$$\Phi_0(t) = V_0 \cos(\Omega t). \tag{2.62}$$

The resulting RF potential confines ions in radial direction under the correct parameters and corresponds to a 2-dimensional Paul trap as shown in Figure 6. In order to expand the 2D confinement to 3D, the 4 hyperbolic electrodes are separated into 3 sections and a direct current (DC) is applied to the outer electrodes at a distance z_0 to the center of the trap. The resulting potential is able to confine ions in axial direction and can be approximated by:

$$\Phi_{\mathrm{DC}}(x, y, z) = \frac{\kappa U_{\mathrm{DC}}}{z_0^2}\left(dx^2 + ey^2 + fz^2\right), \tag{2.63}$$

with $\kappa < 1$ as a geometrical correction factor. Using the Laplace-equation leads to $d+e+f = 0$ and $d = e = -1/2$, $f = -2d = 1$. The potential near the center of the trap can be calculated by adding both RF and DC components:

$$\Phi_{\mathrm{Paul}} = V_0 \cos \Omega t \frac{x^2 - y^2}{r_0^2} + \frac{\kappa U_{\mathrm{DC}}}{z_0^2}\left(-\frac{1}{2}\left(x^2 + y^2\right) + z^2\right). \tag{2.64}$$

Ions inside the trap experience forces that drive them, on average and with suitable parameters, towards the trap center, following the the equations of motion:

$$\ddot{x} + \left(-\frac{qe\kappa U_{\mathrm{DC}}}{mz_0^2} + \frac{2qeV_0}{mr_0^2}\cos(\Omega t)\right) x = 0, \tag{2.65}$$

$$\ddot{y} - \left(\frac{qe\kappa U_{\mathrm{DC}}}{mz_0^2} + \frac{2qeV_0}{mr_0^2}\cos(\Omega t)\right) y = 0, \tag{2.66}$$

$$\ddot{z} + \frac{2qe\kappa U_{\mathrm{DC}}}{mz_0^2} z = 0. \tag{2.67}$$

Following the notation used in 2.1 q denotes the charge state. Nonetheless, the quadrupole potential needs to be fine tuned for the targeted ion in order to trap it. Whether or not the potential is going to be able to confine the motion of an ion depends on its q/m ratio. This means that different particles need to have very similar q/m ratios in order to be stored at the same time. This is only possible within the adiabatic approximation where $a_u, q_u \approx 0$

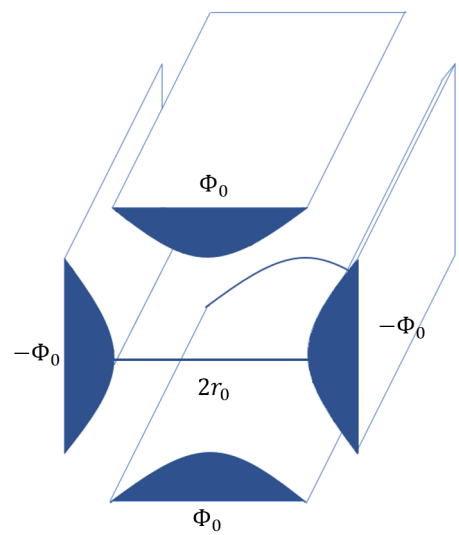

Figure 6: Sketch of the hyperbolic electrodes used for the RF-potential. Φ denotes the potential applied to the electrodes and r_0 the distance between the trap center and the electrodes.

[13]. The equations of motion Equation 2.65-2.67 can be recognized to be in the form of the Mathieu equations

$$\frac{d^2}{d\xi^2}u + (a_u - 2q_u \cos 2\xi)\, u = 0,\ u = x, y, z, \tag{2.68}$$

with the parameters:

$$a_x = a_y = -\frac{1}{2}a_z = -\frac{4qe\kappa U_{\mathrm{DC}}}{mz_0^2\Omega^2}, \xi = \frac{\Omega t}{2}, q_x = -q_y = \frac{4qeV_0}{mr_0^2\Omega^2}, q_z = 0 \tag{2.69}$$

Note the difference between q and q_u, being q the charge state of the ion and q_u the parameter from the Mathieu equations. The solutions of the Mathieu equations are divided in stable and unstable ion trajectories as shown in figure 7. The stable trajectories bind the motion of the ion within the trap while the unstable trajectories end up with the ion in question flying away. Paul traps are generally operated in the stable regions closest to $a_u = q_u = 0$ [13].

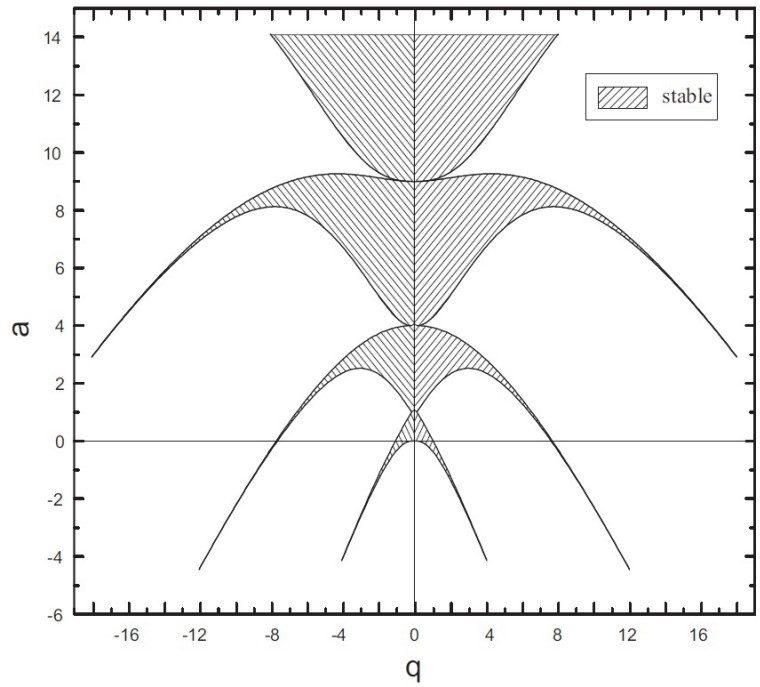

Figure 7: Stable regions for $a = a_x = -a_y$ and $q = q_x = -q_y$. Taken from [13].

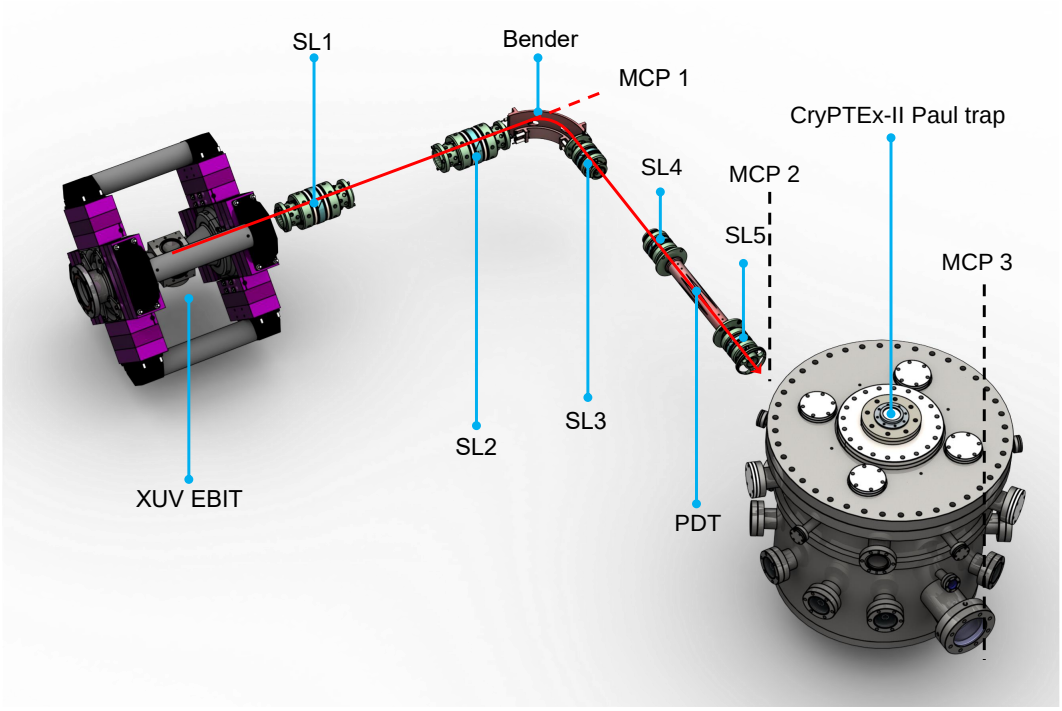

Figure 8: CAD model of the whole beamline, including the EBIT and the Paul trap. The trajectory of the ion bunch is shown in light blue, while the alternative trajectory, with the bender turned off, is shown as the dotted light blue line. The placement of the MCPs is also shown, although the second one can be retracted using a manipulator, opening the path towards the Paul trap. The position it would take in the beamline is shown by the dotted black line.

3 Experimental setup

The experiment is divided in three parts: the XUV EBIT [11], the beamline and the CryPTEx-II Paul trap [13]. The beamline is based on the one used by L. Schmoeger [22], [24] at CryPTEx-I, developed by P. Micke [25] and built by M.K. Rosner [26]. argon neutrals are injected to the XUV EBIT where an electron beam with energies up to 6 kV produces boron-like argon operating at a beam energy of 1.175 kV. The beamline consists of five Sikler lenses (SL) that steer and focus the extracted ion bunch, one electrostatic benders and an electrodynamic pulsed drift tubes (PDT). In order to perform diagnostics, three micro-channel plate (MCP) detectors are used. After passing the beamline, the ion bunch arrives at the CryPTEx-II Paul trap to get re-trapped. This chapter will go through the relevant parts of the experiment and their practical functionality.

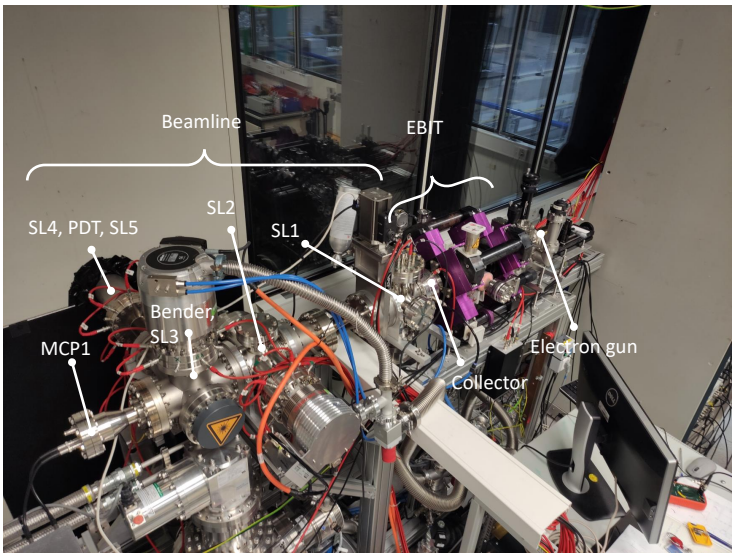

Figure 9: Picture of the experiment setup, showing the room in which the EBIT and the beamline are located.

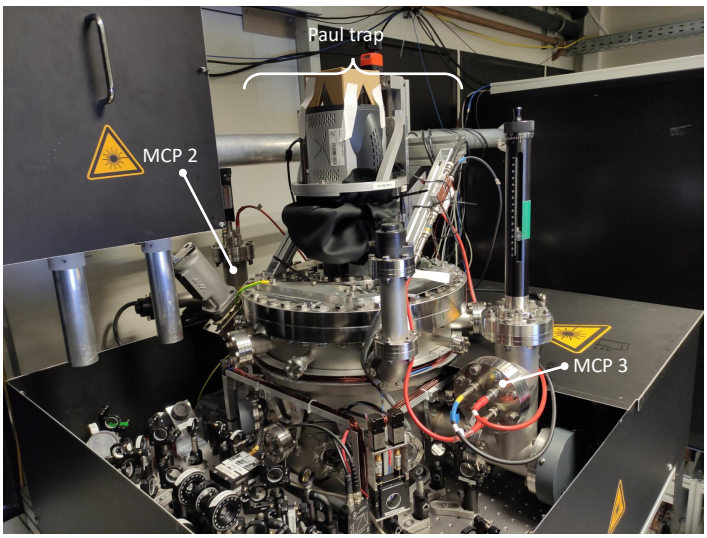

Figure 10: Picture of the setup at the Paul trap. Only the relevant and visible parts are marked.

3.1 XUV EBIT

The XUV EBIT is a Heidelberg compact-type EBIT [11] capable of ionizing neutrals multiple times and trapping the produced ions, thus becoming a reliable supply of HCIs. The machine consists of an electron gun, six drift tubes, a collector, an injection system and a magnetic structure. The beam energy ranges between 100 V and 6 kV, while here an energy of 1.175 kV was used to maximize the Ar^{13+} yield.

3.1.1 Magnet assembly

The structure consists of a combination of 72 magnets assembled as two cross shapes connected by the tips. Due to irregularities in the yoke, additional magnets were added to improve the transmission of electron inside the EBIT. This structure is responsible for compressing the electron beam.

3.1.2 Drift tubes

Six drift tubes (DT) inside the XUV EBIT are responsible for trapping the ions and optimizing the transmission through the EBIT. DT1 and DT2 are tasked with the electron beam, since they can focus the beam in the direction of the trap center. Meanwhile DT4 determines the energy of the electron beam, with DT3 and DT5 set at higher voltages to produce the potential well at the forth drift tube. The well has to be deep enough to trap the lesser ionized ions, since the potential has a smaller effect on them. Then the potential at DT4 is lifted, inverting the trap at a given time t_{kick} to extract the ions, typically for a few μs. This process is repeated with a frequency $f_{\text{kick}} = 3\,\text{Hz}$ for a maximized yield of the desired Ar^{13+}. Then the last drift tube, DT6 is optimized for the transmission of the electron beam. During this work DT6 was it not being necessary.

3.1.3 Electron gun and collector

The electron gun consists of three electrodes: cathode, focus and anode. The cathode is heated up to temperatures close to 1000 °C bringing the electrons to the Fermi-band, lowering the work needed to emit them Φ_{emission}. The electrons are then focused and accelerated by the positive potentials of the focus and anode electrodes. After leaving the electron gun, the electron beam would scatter itself due to its emittance, but due to the before-mentioned magnetic structure, it stays focused and gets compressed through the drift tubes. Once the beam leaves the drift tubes, it reaches the collector. It consists of

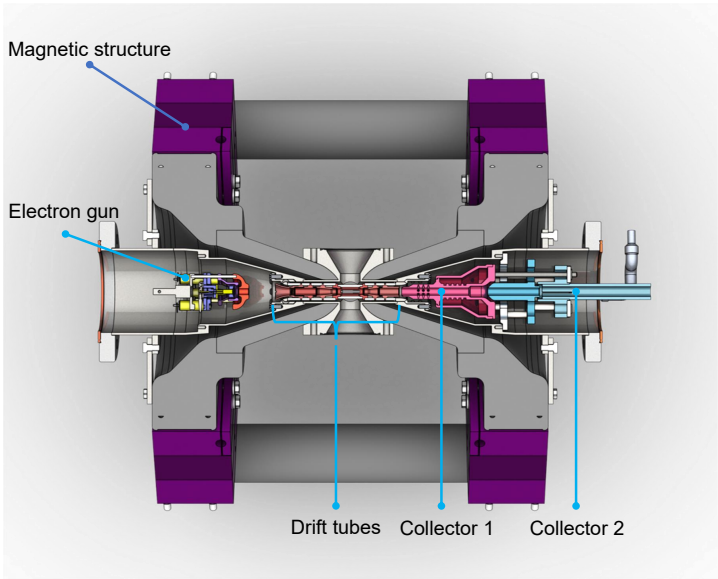

Figure 11: Cross section of the CAD model of the EBIT showing its different components.

three different electrodes: the first and second extraction tubes and the collector electrode. The assembly is shown in Figure 11. The beam reaches the collector electrode, which is grounded, and is slowed down. In addition to that, the magnetic field vanishes in the collector region, which expands the beam. Finally, the first extraction tube is set to a more negative potential than the cathode, thus preventing the electron beam to leave the trap. The second extraction tube is not necessarily tuned in regard to the electron beam, but can rather be used to maximize the ion yield of the EBIT.

3.2 Beamline

The beamline is set to transport HCIs from the XUV EBIT to the Paul trap while selecting a specific charge state and decelerating the beam. It consists of a total of 5 Sikler lenses, a bender and a pulsed drift tube. In addition to that, a vacuum system is put in place, for more details about it refer to [26]. This beamline is a further development of the one designed by L. Schmöger [22], [24], developed by P. Micke at the Physiklaisch-Technische Bundesanstalt Braunschweig in a collaboration with the Max-Planck-Institut für Kernphysik [25] and built during the Master's thesis of M. K. Rosner [26].

3.2.1 Sikler lens

A Sikler lens (SL) consists of four electrodes that can act as an einzel lens. These electrodes are placed as shown in Figure 12. During this work, the electrodes are named after their position in the direction of the ion beam in German: Links-Oben (LO, Top-Left in English),

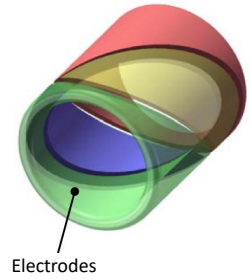

Figure 12: Part of the CAD model of a Sikler lens. Taken from [26]. LO corresponds to red, RO to yellow, BR to green and BL to blue

Rechts-Oben (RO, Top-Right), Links-Unten (LU, Bottom-Left) and Rechts-Unten (RU, Bottom-Right). Due to the geometry of the Sikler lens, these four degrees of freedom can be used for three purposes (two degrees of freedom are used for steering) without changing the energy of the ion beam:

1. **Focus:** By giving all electrodes a certain potential the resulting quadrupole field has the form of a potential well with the well at the center of the lens, acting as an einzel lens.

2. **Steer:** By biasing a pair of neighboring electrodes with different potentials the produced electric field exerts a force in radial direction defined by the set voltages. Biasing LO and RO to a higher potential than LU and RU would steer the beam towards the bottom part of the beamline and otherwise. The same applies horizontally in both left and right directions.

3. **Astigmatism:** Similar to light in an eye, an ion beam can also suffer aberrations in which ions (photons in an eye) that come from different planes are focused to separated points. For example, a circular beam could become elliptical if the astigmatism is not addressed. In order to correct this effect, opposite electrodes, i.e. LO+RU and RO+LU, can be set to the same potential similar to the steering process.

3.2.2 Bender

A 90° bend was chosen in order to fulfil the spatial requirements given by the lab and to give optical access to the principal Paul trap trapping axis. The bender is tasked with steering the ion beam so that the majority of the ion beam gets pass this curve without loosing too many ions. It consists of two hollow cylinders of different height and radius that are placed at typically, disparate potentials. The geometry of the bender makes the produced electric field act with a focusing effect. Moreover, the bender has an opening that allows the ion

beam to fly straight towards the first MCP (MCP1) in case the bender is turned off. SL3 is mounted right after the bender to correct possible miss-steering of the ion beam while in the bender and allow an easier optimization of the bender. The typical voltages applied to both the bender and SL3 range between $< 100\,\mathrm{V}$ up to around $500\,\mathrm{V}$, depending on the extraction energy. The optimized voltages are shown in Table 4 under chapter 4.3.

3.2.3 Pulsed drift tube

Perhaps the most important element of the whole beamline, the pulsed drift tube (PDT) is tasked with the deceleration and bunching of the ions. It consists of two serrated drift tubes assembled next to each other as shown in Figure 13. This connection produces an almost linearly increasing potential in axial direction around the middle of the PDT. In order to achieve such a potential, each tube has to be set to a different voltage, with the first one (PDT1) being at a lower voltage than the latter one (PDT2). Their geometry also affects the beam like an einzel lens (i.e. it focuses the beam) and makes the faster ions experience a higher voltage in the serrated part. This accomplishes a narrower energy distribution and a more focused beam. The resulting potential along the beam axis is shown in Figure 14. The typical set voltage corresponds roughly to $\Phi_{\mathrm{kick}} - 200\,\mathrm{V}$, so that the ion bunch ends up in the range of the elevated ground (see chapter 3.3).

3.2.4 Diagnostics

Since the goal of the experiment is to get ions to the CryPTEx-II Paul trap using numerous degrees of freedom, a system of diagnostics that allows to calibrate each degree of freedom to optimize the ion beam is needed. As discussed in chapter 2.2.1, the main way to differentiate charge states is their time of flight, which makes a diagnostic system based on time resolution with a resolution up to 100 ns necessary. This is why micro-channel plate detectors with resolutions up to the ns regime were built at the beamline. Three of them are placed along the whole experiment as shown in Figure 8, which give feedback at each important stage of the beamline: straight out of the EBIT, before the Paul trap and after the Paul trap.

The used MCP detectors consists of two plates with numerous parallel very thin channels with a diameter of around $50\mu m$, tilted 8°, made out of a electrical resistant material ($\approx 100\Omega$). Once an ion enters through a channel, it will eventually hit the wall and cause the emission of secondary electrons which will end up in a cascade effect, thus acting as an electron multiplier. A single plate would achieve a signal magnification of $\approx 10^3 - 10^4$, but by setting the two plates in the so called Chevron configuration ($\bigwedge$), it allows a signal magnification up to 10^7 [27].

The second and third MCP detectors do have slight variations in regard to the first one.

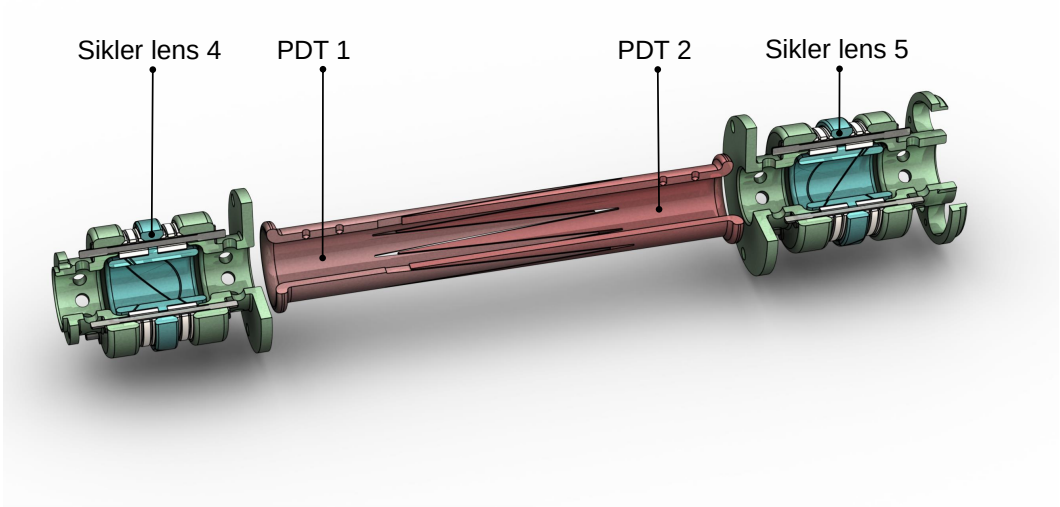

Figure 13: Render of the CAD model of the pulsed drift tube and its two adjacent Sikler lenses. The fourth Sikler lens steers the ion beam towards the center of the pulsed tube, which consists of two serrated drift tubes. PDT1 is set to a lower voltage than PDT2. This slows down the ions while focusing them. The fifth Sikler lens steers the decelerated beam towards the center of the CryPTEx-II Paul trap.

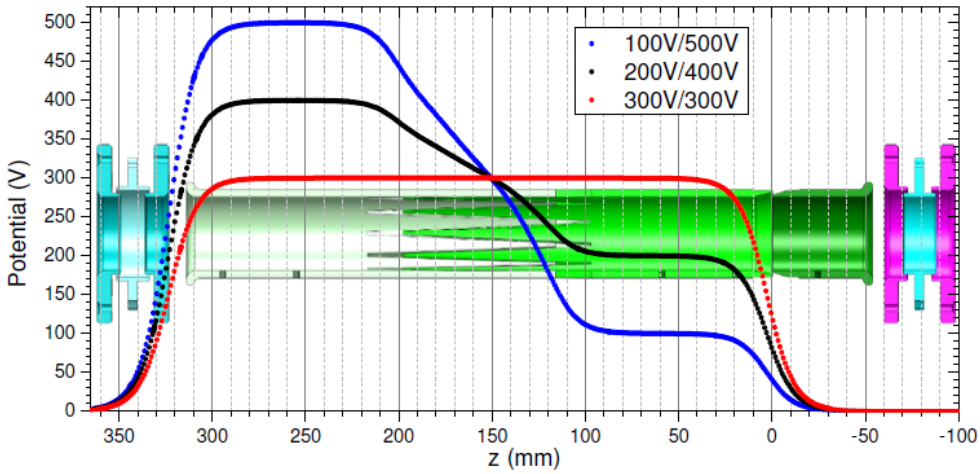

Figure 14: Potential along the beam axis inside the pulsed drift tube simulated with SIMION by L. Schmöger. The linear increase lies in the middle of the pulsed drift tube, between approximately 100 mm and 200 mm. The center of the pulsed drift tube is at the 150 mm mark. Taken from [22].

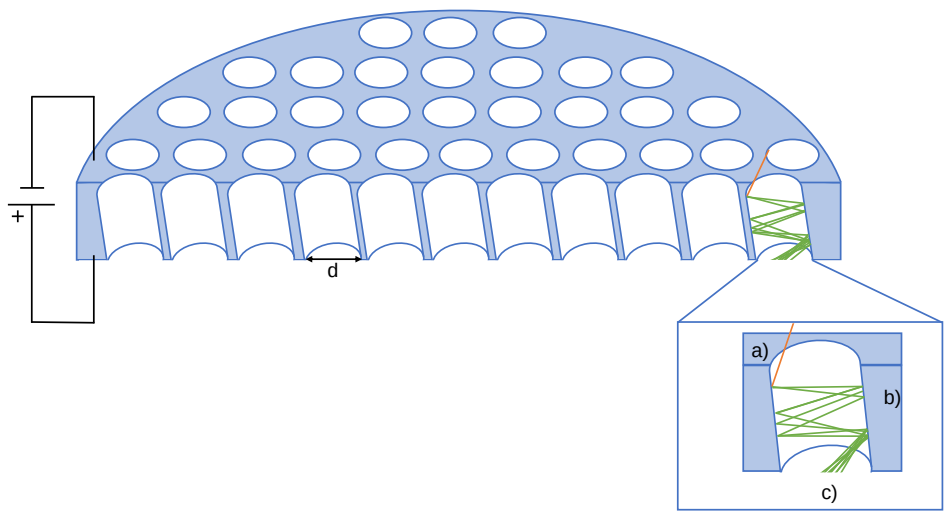

Figure 15: Schematic of the functionality of an MCP: a) Incoming ion. b) Secondary electrons displaced by the ion. c) Electron cascade that falls onto the detector. d denotes the diameter of the holes, which corresponds to $50\mu m$.

While the first one is placed at fixed location (i.e. there is no way of moving it without disassembling parts of the beamline), the second and third MCP detectors can be moved with their respective linear manipulators to let the ions fly pass or adjust their optimal placing. The second one is also equipped with a retarding field analyzer that consists of two grids. The first one is grounded while the latter is set to the positive potential Φ_{Grid}. Ions with an energy smaller than $qe\Phi_{\text{Grid}}$ do not reach the MCP, while more energetic ions do reach it. This enables the measurement of the energy-distribution of the ion beam.

3.2.5 Timing of the beamline

Different elements of the beamline need to be pulsed with high precision in order to achieve the selection of Ar^{13+} and the energy reduction at the PDT. For that regard, two different signal generators are used. The first one is a gated delayed generator (by Stanford Research Systems, INC., Model DG535) which is tasked with the extraction of the EBIT by sending a pulse at $t = D$. Then, it also send a square-pulse to SL3O, so that it is turned off all the time, except for the set selection window. This window begins at the time $t =$ open and ends at $t =$ close. The gated delayed generator also sends a pulse at $t = T_0$ towards the second signal generator, an Agilent 33522A 30 MHz Function/Arbitrary Waveform Generator (from now on signal generator). This one is tasked with the bunching of the ions by the PDT, sending a pulse at $t = C$, and with the control of the mirror electrodes via switching between

elevated ground and Φ_{Mirror}.

All the mentioned pulses go to fast voltage switchers (model GHTS fast high voltage push-pull switch by Behlke and model Behlke HTS-31-03-HB-C by the Max Planck Institut für Kernphysik). These have three inputs and one output. The inputs are "+ voltage", "-voltage" and "trigger control". By switching the polarity of the instrument, one of the voltages is set as the output. Once the trigger signal arrives, the Behlke will switch its output from the default voltage to the other one for as long as the trigger signal keeps coming. This can be set by adjusting the pulse width on the signal-generators. The typical trigger signal for a Behlke is a square-pulse with $\approx$ 1V positive offset and $\approx$ 2Vpp (Volt from peak to peak).

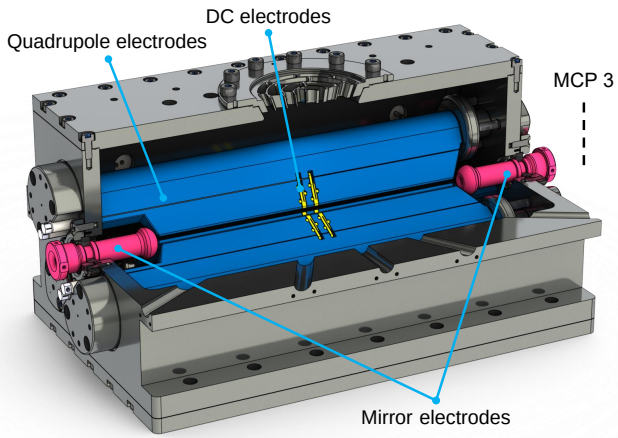

Figure 16: Cross section of the CAD model of the CryPTEx-II Paul trap, showing the mirror electrodes in pink, the DC and RF electrodes in yellow and blue respectively as well as the location of the third MCP. The distance between both mirror electrodes is 115 mm.

3.3 CryPTEx-II Paul trap

In this chapter the relevant parts of the CryPTEx-II Paul trap will be described. In Figure 16 a cross section of the Paul trap is shown. The electrodes inside the Paul trap can be separated in three classes: rf electrodes, dc electrodes and mirror electrodes. As their names imply, the rf and dc electrodes are used to produce the respective rf and dc electric fields, that, on a timely average, end up generating the potential well for trapping ions. The mirror electrodes are tuned as part of the beamline and are tasked with the focusing of the ion bunch and the so called re-trapping. The setup is constructed in such a way that the electrical ground of the trap is isolated from the surrounding vacuum chamber, so that a common bias can be applied to all the voltages of the trap. By increasing the bias of the trap, the ion bunch loses a considerable amount of energy when entering, leading to energies in the order of the 10 eV. The trap is set up so that Ar^{13+} and $^{9}Be^{+}$ ions can be trapped simultaneously, so that the beryllium ions can sympathetically cool the highly charged ions. A more in depth description can be found in [13].

Quadrupole electrodes

Four blade-style shaped electrodes constitute the rf electrodes. Their applied voltage V_0 defines the parameters $q_{x,y}$ following Equation 2.69. Since the Paul trap is operated in the first stable region for Ar^{13+}-like ions (see Figure 7), the voltage is set up so that $0 < \|q_{x,y}\| < 0.908$ while $\|a_{x,y}\| \ll 1$. For ground state cooling to be possible, a radial secular frequency on the order of 1 MHz is needed. The RF voltage V_0 needed to reach this secular frequency depends on the resonance frequency of the resonator, which is about $\Omega \approx 34\,\mathrm{MHz}$

DC electrodes

Inside the quadrupole electrodes, eight dc electrodes are mounted in at a distance $z_0 = 2.05\,\mathrm{mm}$ from the trap center. The produced potential traps the ions in axial direction and allows high axial secular frequencies in the order of $f_z = 1\,\mathrm{MHz}$ at relatively low voltages around 25 V. Each electrode can be biased independently, allowing for corrections to the motion of the trapped ions. Additionally, the electrodes were built such that there would be a high capacitance between the dc electrode rods and the quadrupole electrodes which means that the dc electrodes will pick up a considerable fraction of the rf voltage. This feature allows for a more efficient transit of the HCIs since a purely electrostatic potential would mean a drastic loss in ions due to the low radial confinement that would be produced at the location of the dc electrodes.

Mirror electrodes

Finally, two mirror electrodes are mounted on both sides of the Paul trap (see Figure 16). Both electrodes are set up at a distance of 155 mm from each other and are switched to a high voltage of about 200 V to close the trap once the ions enter it, thus making re-trapping possible. Both electrodes have a resistance of the order of 40 MΩ attached to their circuit, forming a RC-circuit in a very simplified approach. With capacitances of the order of 1 pF, the time constant $\tau = RC$ corresponds to approximately 40 µs.
It is also worth noting again that the entire trap can be biased through the so-called elevated ground, which effectively raises the entire trap to a set voltage, typically $\Phi_{\text{ground'}} \approx E_{\text{ion}}/eq$. This slows the ions further down to $E'_{\text{ion}} \approx 1\,\mathrm{eV} \times q$. With this energy the Ar^{13+} ions would fly through the trap with a velocity of around 8.000 m/s. With a distance of 115 mm between the mirror electrodes, the ions would need approximately 20 µs to fly from the first electrode

to the second one and back. Taking into account that the electrodes would only need to load up $\approx 10\,\mathrm{V}$, the process of closing the trap would take $< 10\,\mu\mathrm{s}$, making re-trapping a feasible goal.

Cathode	Focus	Anode	DT1	DT2	DT3	DT4	DT5	DT6
-650 V	-950 V	+300 V	+200 V	+540 V	+570 V	+530	+570 V	0 V

Table 1: Voltages applied to each drift tube of the XUV EBIT. However, the measured voltage at the sixth drift tube was around $\approx$ 30V due to a short-circuit. The EBIT still worked the intended way, so this was ignored.

4 Optimisation of the beamline

The optimisation of the beamline was done in a very systematic way. Starting with the EBIT, every part of the beamline was fine tuned while keeping an eye on the signal at the respective MCP. The first MCP was used to identify the charge states based on their respective time of flights and as a control later on in case no signal was to be found in the second MCP. At the second detector the selection of Ar^{13+} was measured as well as the bunching of that charge state. Lastly, the focus of the beam inside the Paul trap was adjusted using the last MCP.

4.1 XUV EBIT electrodes

First of all, the EBIT was optimized so that an approximately 98% transmission rate between cathode and collector was accomplished while staying close to 10 mA current and 1.15 kV beam energy. This set up maximizes the efficiency of the EBIT and its Ar^{13+} yield.
The drift tubes DT3-4-5 define the potential well in which the ions are trapped and are the biggest factors when tuning the beam energy. By reducing the depth of the well, only the higher ionized species would stay for long, since the exerted force by the trap is proportional to the charge state. The kick-voltage was set at a very low value in order to avoid decelerating the ions too much, since that process would lose too many ions.

4.2 Charge state identification

After getting a constant and reliable ion yield, SL1 and 2 were optimized to maximize the signal at the first detector. The rest of the optical elements were turned off during this process, with the EBIT operating with the before-mentioned settings in addition to the ones shown in Table 2. By raising the fourth drift tube to Φ_{kick} at different frequencies, multiple charge states are produced as shown in Figure 17.
After extracting the time of flight of each charge state by fitting multiple Gaussians, the charge state can be inferred by fitting Equation 2.32 to the time of flight profile. This was done after summing multiple spectra from frequencies between 1 Hz and 50 Hz, in order to analyze the times of flight of more charge states and hence improve the confidence of the

Extractor 1	Extractor 2	Kicker Φ_{kick}
2.54 kV	0.84 kV	692 V

Table 2: Extraction voltages of the XUV EBIT. Φ_{kick} defines the energy with which the ions leave the trap, while both extractor potentials are tuned to optimize the signal at the MCP.

SL1LO	SL1RO	SL1RU	SL1LU	SL2LO	SL2RO	SL2RU	SL2LU
121.3 V	185 V	142 V	233 V	273 V	197 V	156.5 V	296 V

Table 3: Voltages applied to each electrode of the first two Sikler lenses.

fit.

The results show the presence of charge states ranging from Ar^{10+} up to Ar^{16+}. By comparing the beam energy (1.175 kV) to the ionization energies of the different charge states (see Table 8), this is to be expected. The big difference in the ionization energy between Ar^{16+} and Ar^{17+} is due to the 17th and 18th electrons being in the 1s shell. Once the ionization states were identified, the extraction rate was set at 3 Hz as the optimal extraction rate for Ar^{13+}.

4.3 Charge state selection

The bender and the third Sikler lens were optimized using the second MCP before the Paul Trap in order to start the charge state selection. Sikler lenses four and five were reserved for the slowing mechanism and the optimization behind the trap. The voltages applied on the bender and the Sikler lens are shown in Table 4.

Before finally selecting the desired charge state, Ar^{13+}, the time of flight measurement was repeated in order to confirm the results from the first MCP. The optimization of the beamline enabled the recognition of the same time of flight spectrum, as shown in Figure 19. By fitting the same functions as before, the results are clear. The yield of Ar^{13+} is indeed maximized for an extraction rate of 3 Hz and the time separation of the different charge states is high enough to select one of them without severely hindering the signal of the desired one. This process is done by putting an electrode of a Sikler lens at ground potential by default and switching the voltage to the optimal one in a small window of around 200 ns, so that all charge states are deflected from the beamline except for the desired one. Due to a short circuit between the third Sikler lens and the bender, the optimization of the ion beam was not completely possible, which made the beam very sensible to small differences in the potentials set. For this reason, SL3O was selected as the kicker electrode, leading to good results as shown in Figure 21. The beginning of the selection windows was set at

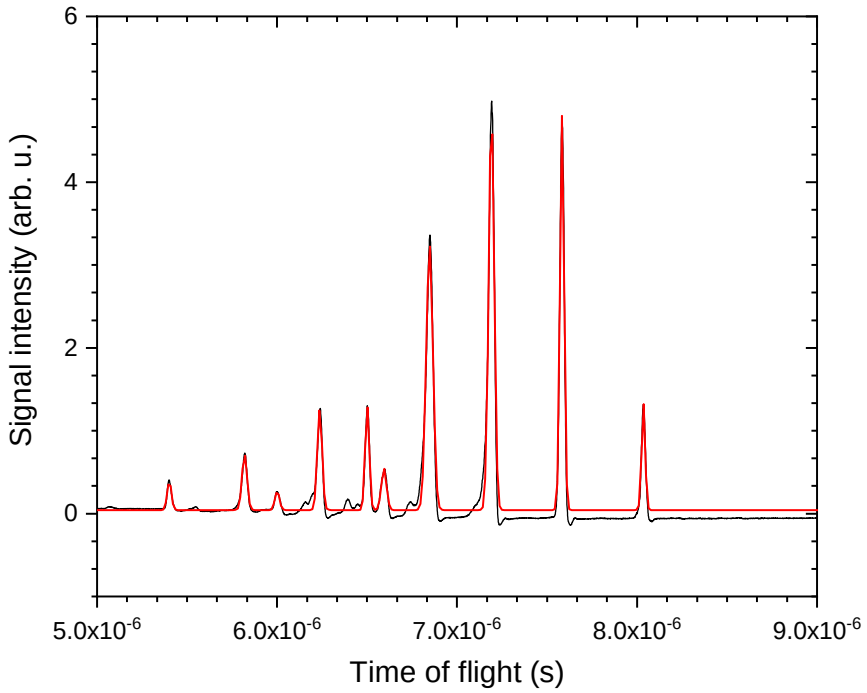

Figure 17: Time of flight spectrum for an extraction frequency of 10 Hz with a multiple Gaussian fit (red) applied to the signal (black).

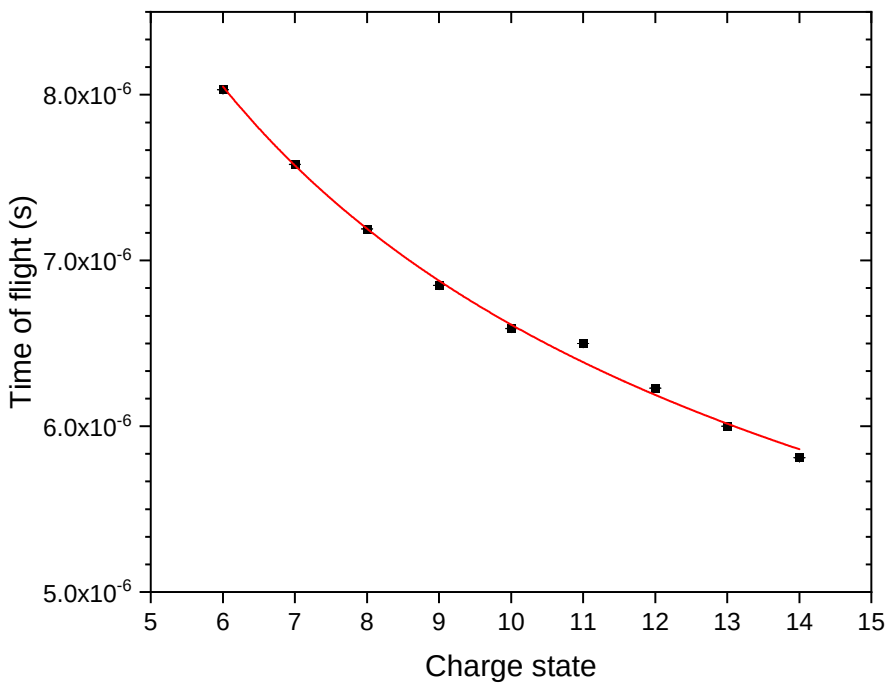

Figure 18: Times of flight plotted against their respective charge states (black dots). The peaks that do not correspond to argon charge states were ignored. The function described in Equation 2.32 was fitted to the data using σ from each Gaussian as the error for plot.

SL3L	SL3O	SL3R	SL3U	BEND+	BEND-
120 V	170 V	140 V	240 V	140V	-176V

Table 4: Voltages applied to the third Sikler lens and the bender (BEND). There is a short-circuit between BEND+ and SL3R, so the rest of the optical elements were tuned in order to circumvent this issue. Due to the high sensitivity of the beam in regards to SL3, the upper electrode (SL3O) was tasked with the selection of the charge state.

$t_{\text{open}} = 6.13\,\mu\text{s}$ and its end at $t_{\text{close}} = 6.36\,\mu\text{s}$. The overlap between the selected charge state and the identified Ar^{13+} confirms the success of this selection.

4.4 Slow down of ions

Once the charge selection was successful, the next goal was to lower the energy of the ions to $< 200 \times q \times e\text{V}$, in order to get the ions into the range of the elevated ground. This is achieved by setting the pulsed drift tubes to $\Phi_{\text{low}} = 420\text{V}$ and $\Phi_{\text{high}} = 580\text{V}$ and switching them to ground at the right time. By scanning the switching time in small steps ($\sim 10\,\text{ns}$) (i.e. taking a time of flight signal for a range of switching times), a profile can be distinguished. Before discussing the profile a small technicality is due: the trigger signal sent to the pulsed drift tubes was a square signal with a pulse width of 9.998 μs. This pulse makes sure that the pulsed drift tubes are turned on again once the ions are long past the tubes and have already reached the MCP before the trap, thus having no further effect on the trajectory after being turned off. The profile is shown in Figure 13 and it can be divided into several segments:

(a) The ions have not reached the PDTs yet. They fly through the tubes without experiencing any of the set voltages and their energy stays close to $qe \times \Phi_{\text{kick}} = 700\,\text{V}$.

(b) The signal drops in intensity due to the selection of the faster ions. They get into PDT1 while the slow ones are still at SL4 or even further away. The energy at this point is measured to be $\approx 620\,\text{V} \times qe$ (see chapter 4.5), which backs up the assumption that the higher energetic ions are gone.

(c) Even the slow ions are caught entering PDT1 and begin to experience Φ_{low}. There is a clear increase in the time of flight of approximately $1.2\,\mu\text{s}$.

(d) The ions find themselves in the plateau present at the first PDT. They have not reached the serrated part of the tubes yet and their energy corresponds roughly to $E' = qe(\Phi_{\text{kick}} - \Phi_{\text{low}}) \approx 200\,\text{V}qe$.

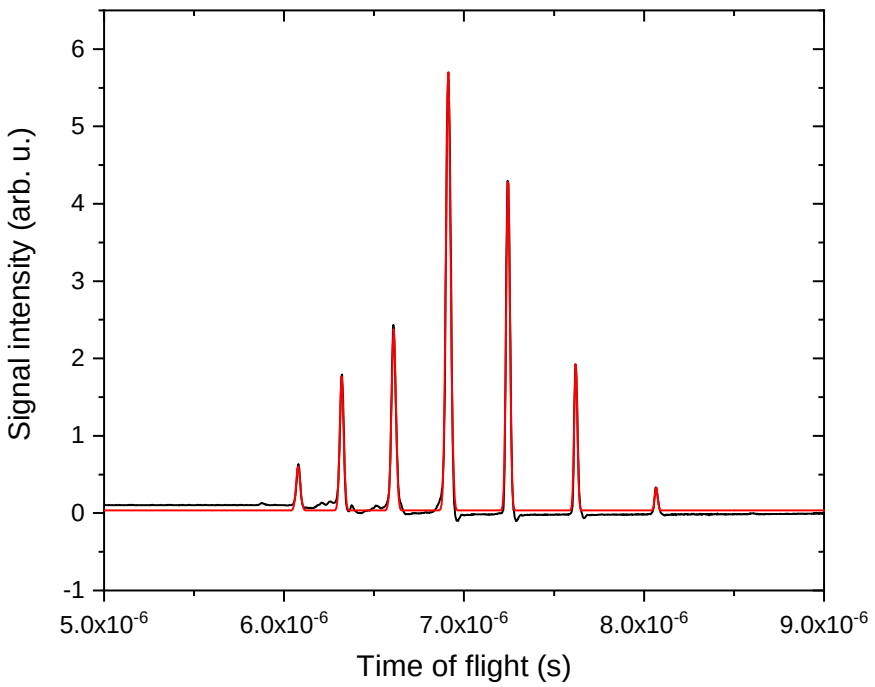

Figure 19: Spectrum of the time of flight taken for an extraction rate of 6 Hz (black) with a multiple Gaussian fit (red) to determine the location of each peak.

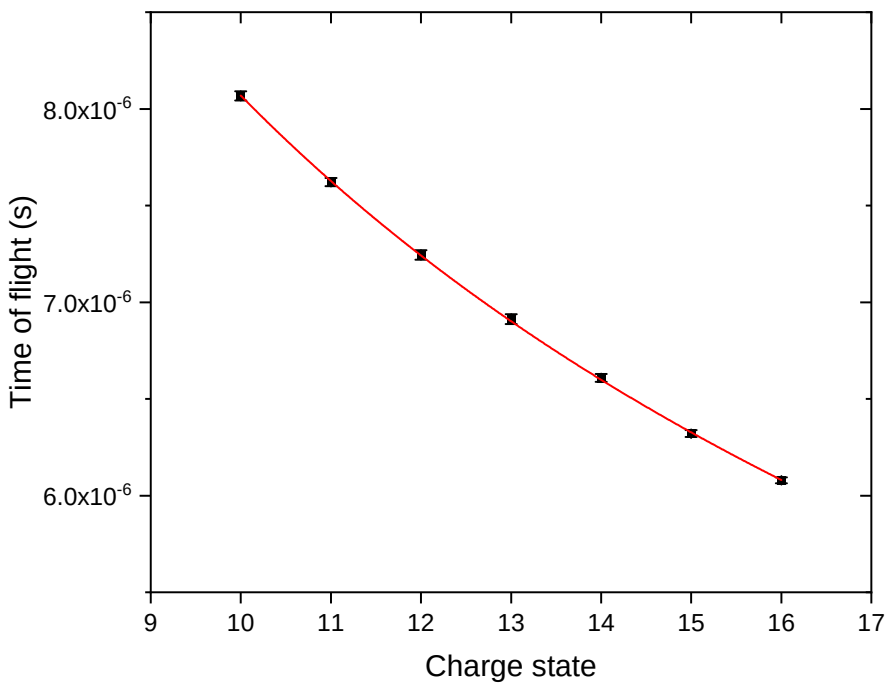

Figure 20: Each time of flight plotted against their charge state with a time of flight fit (see Equation 2.32) to confirm their charge state. Despite the newly presence of Ar^{15+} and Ar^{16+}, the identification is consistent with the measurements at the first MCP. The presence of other elements in the beamline hindered the identification of these charge states at the first MCP, due to overlap between peaks. However, due to the increased path length the Ar^{15+} and Ar^{16+} peaks were distinguishable from the other ones.

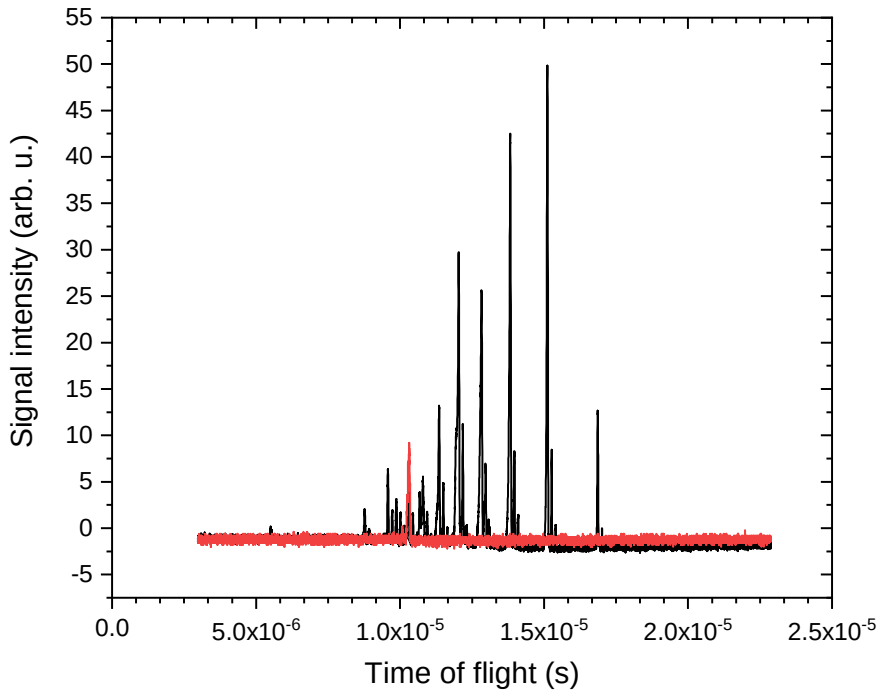

Figure 21: Comparison between the time of flight spectrum with and without selection. The original signal comes from the addition of the spectra at extraction rates between 1 Hz and 50 Hz, while the selection was measured only at 3 Hz. This signal was taken after tuning SL4 and SL5 on, leading to higher times of flights due to the deceleration and acceleration that the ions experience. The potential at the MCP was also raised in comparison to Figure 19, which causes the signal rebounds seen after each peak. The lower signal intensity present for Ar^{13+} is due to its lack of predominance at higher extraction rates (> 10 Hz), making its peak seem smaller in comparison.

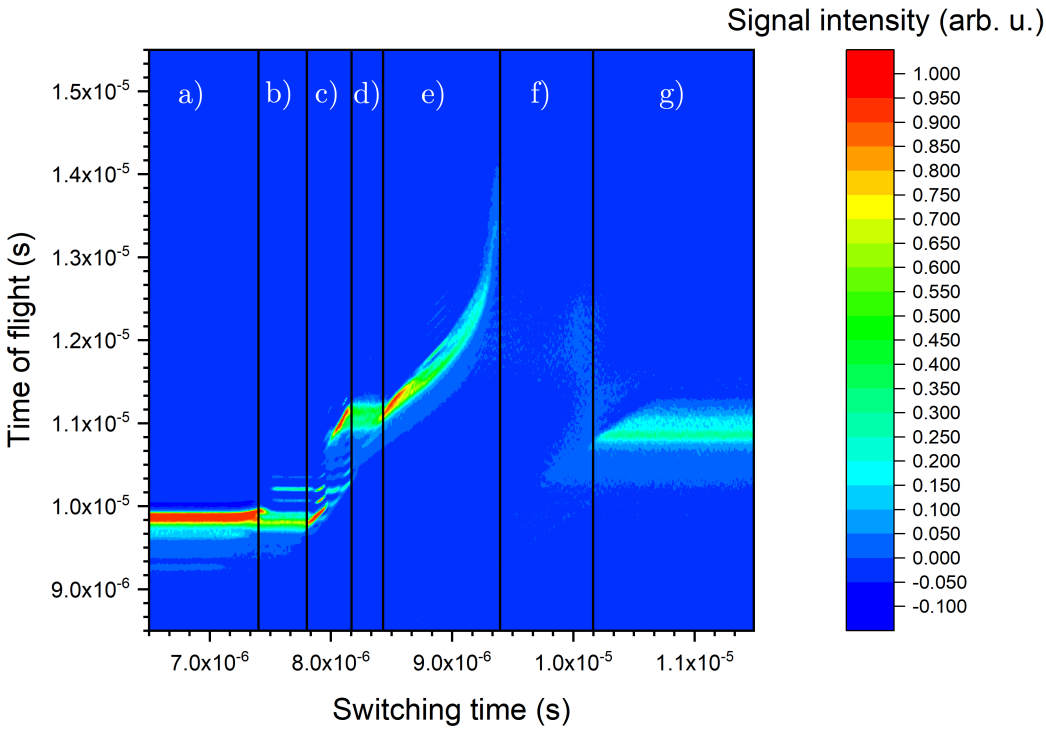

Figure 22: Scan of the time of flight of Ar^{13+} at different switching times for the PDT. The negative intensities are due to saturation of the MCP.

(e) The so-called "ramp" is reached. In this stage the potential inside the PDTs increases linearly up until Φ_{high} is reached. Ideally, the PDTs would be turned off in the middle of this stage. Since the time of flight is inversely proportional to the velocity of the ions and they reach relatively slow velocities, the $1/v$ tendency is very clear at the end of this stage.

(f) A plateau is expected at this stage, since the ions would find themselves in the middle of PDT2. However, Φ_{high} is very close to E_{ion}/qe, making the ions fly very slowly, hindering the signal significantly.

(g) The ions successfully fly through the PDTs while they are still on and regain their energy back before the tubes are turned off. They have a longer time of flight than the ions of stage a) because they are decelerated and accelerated again (to their original speed), lowering their mean velocity.

Another remark about the segment e) is the key difference between different ion energies. Since the time of flight is inversely proportional to the velocity of the ions and hence, to

SL4LO	SL4RO	SL4RU	SL4LU	PDT1 Φ_{low}	PDT2 Φ_{high}	$\overline{\text{PDT}}$
122 V	122 V	118V	208V	420 V	580V	500 V

Table 5: Voltages applied to the fourth Sikler lens and the pulsed drift tubes. The similarity in the voltages of the Sikler lens show the importance of focusing the beam towards the center of the pulsed drift tubes and the already good focus after SL3.

their energy, a linear approximation is appropriate for a high energies. However, such an approximation loses validity in the lower regime, due to the nature of the $1/x$ functions. In the segment the transition of the validity region of the linear approximation is patent and the reason for the curve at the end of the "ramp".
Segment e) is also of interest because the ideal switching time t_s lies within it, at which the faster ions will have experienced a higher potential than the slower ones, thus narrowing their energy distribution and making the ion bunch more manageable for re-trapping.

4.5 Energy analysis

After finding the ideal time range at which the PDT shall be turned off, the determination of the exact switching time was due. In order to do so, the energy of the ion bunch was first measured at $t_s = 7.748\,\mu\text{s}$ by measuring the signal intensity as a function of the voltage set at the retarding field analyzer. Ions with a higher energy ($E_{\text{ion}} > qe\Phi_{\text{grid}}$) would fly past to the MCP while the lesser energetic ones would be blocked. Assuming a Gaussian distribution for the energy of the ions, this measurement shows the cumulative signal, i.e. the integral of a Gaussian distribution. As a consequence, the error function was selected as the fit function:

$$\text{Signal}(\Phi_{\text{grid}}) = A\left[1 - \text{erf}\left(\frac{\Phi_{\text{grid}} - \overline{\Phi}}{\sqrt{2}\sigma}\right)\right] \tag{4.1}$$

However, a selection takes place at the PDT, letting lesser energetic ions fly through. Assuming that the resulting does not have enough time to fully re-thermalize itself and reach the Gaussian distribution, the fit should then not be applied to the whole curve but only to the slower part of it. In order to test this assumption, three fits were made: one up to $\Phi_{\text{grid}} = 625\,\text{V}$, a second one from then on and a complete one. The results are shown in Figure 23 and the fit parameters are:

1. Complete fit:

$$\overline{\Phi}_1 = 623.10(27)\,\mathrm{V}, \tag{4.2}$$

$$\sigma_1 = 9.60(37)\,\mathrm{V}. \tag{4.3}$$

2. Slow half-fit:

$$\overline{\Phi}_2 = 624.39(41)\,\mathrm{V}, \tag{4.4}$$

$$\sigma_2 = 14.31(63)\,\mathrm{V}. \tag{4.5}$$

3. Fast half fit:

$$\overline{\Phi}_3 = 629.1(11)\,\mathrm{V}, \tag{4.6}$$

$$\sigma_3 = 3.23(45)\,\mathrm{V}. \tag{4.7}$$

This shows that the resulting energy distribution is the result of the overlap between two Gaussian distributions. The reason for the presence of two Gaussian distributions is the division that occurred at PDT1. The faster ions began to experience the voltage of PDT1 before it was turned off, slowing them down. However, the re-thermalization of the ion bunch would be accomplished through ion-ion collisions, which were measured to happen at a rate of 1 kHz inside the Berlin EBIT with a beam energy of 9 keV and a current of 75 mA [28]. Such a rate would correspond to a re-thermalization time in the order of 1 ms, which would be, by far, not enough to re-thermalize the ion bunch in the beamline. Moreover, the circumstances at the beamline produce a way lower ion-ion collision rate, due to the lack of confinement in axial direction. In other words, since the ions are flying through the beamline, it is extremely unlikely that the whole bunch would re-thermalize.
Nonetheless, the energy of the ion bunch before the PDT can be approximated to $\approx 625\,\mathrm{V} \times eq$. The retarding field analyzer was then set to $629\,\mathrm{V} - 500\,\mathrm{eV} = 129\,\mathrm{V}$ and the switching time was scanned until the signal intensity dropped to the half in order to find the optimal switching time t'_s. However, due to a high drop in the signal intensity, it was decided to take a different switching time $t'_s = 9.128\,\mu\mathrm{s}$, at which an energy analysis was done. This is shown in Figure 24 and the results are:

$$\overline{\Phi}' = 139.26(16)\,\mathrm{V}, \tag{4.8}$$

$$\sigma' = 5.79(21)\,\mathrm{V} \tag{4.9}$$

It is clear that the energy distribution gets, in fact, more narrow with the use of the PDT, which improves the probabilities of success at re-trapping highly charged argon.

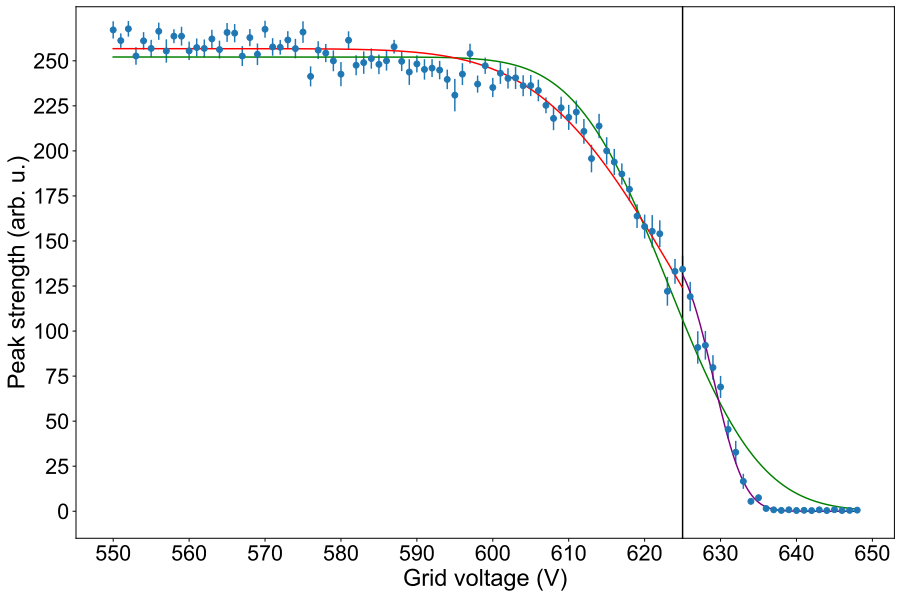

Figure 23: Energy distribution of the ion beam with a switching time of 7.748 µs. The intensity is calculated by integrating each signal and averaging over 128 measurements. The error used was the statistical error. The error function was fitted to the whole curve (green), to the curve below $\Phi_{\text{grid}} < 625\,\text{V}$ (red) and past it (purple).

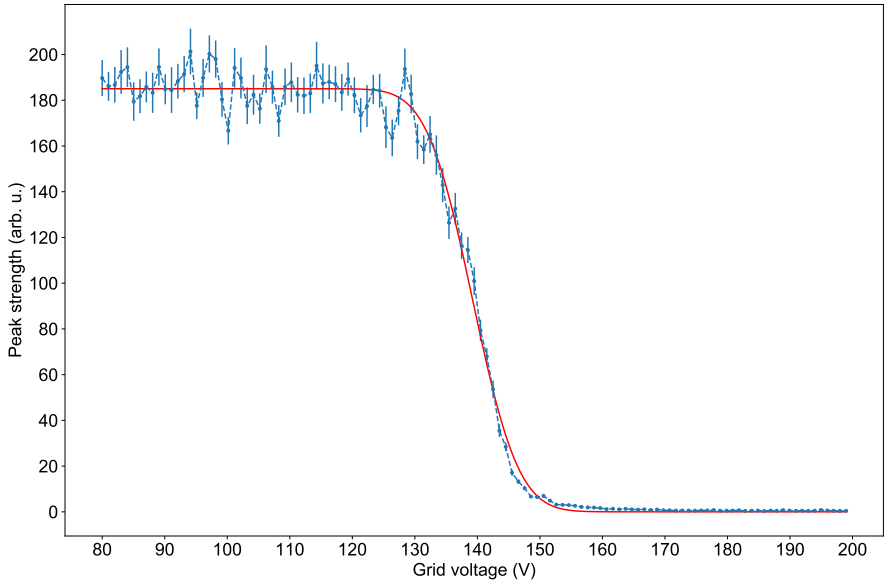

Figure 24: Energy distribution of the ions after switching off the PDT at $t_s = 9.128\,\mu s$. The same procedure in Figure 23 was followed.

4.6 Towards re-trapping of Ar^{13+}

With the ions slowed down, re-trapping can be attempted. First of all, the fifth and last Sikler lens was tuned so that as much Ar as possible would reach the MCP behind the trap. However, not all the pulses were able to reach the MCP despite the optimization of SL5 (for the voltages refer to Table 6). It is important to remark that the optimization was done with the Paul trap already operating. That way, the ion bunch experiences the radio frequency quadrupole field and are further focused.

After directing the HCIs to the MCP, the mirror electrodes were set up with the goal of reflecting the bunch while slowing it further down to $< 10\,eV$ via the elevated ground. Firstly, the voltage set at the mirror electrodes is selected to be $\Phi_{mirror} = 200\,V$ and it was triggered by a pulse with a width of $200\,\mu s$. The signal intensity was then measured dependent on the pulsation-timing of each mirror electrode.

The results shown in Figure 25 and Table 7 indicate that the first mirror electrode lets a maximum amount of ions fly through after being pulsed between $222\,\mu s$ and $127\,\mu s$ before emptying the EBIT (i.e. the mirror electrode is almost turned off between these times). The same measurement was repeated with the mirror electrode behind the trap, see Figure 26. These measurements were carried out without any bias applied to the Paul trap and their

SL5LO	SL5RO	SL5RU	SL5LU
94 V	34 V	65 V	65 V

Table 6: Voltages applied to the fifth Sikler lens to optimize the signal behind the Paul trap.

Mirror 1 start	Mirror 1 end	Mirror 2 start	Mirror 2 end
−222 µs	−127 µs	−215 µs	−153 µs

Table 7: Trigger times between which the signal is not hindered (start and end of the plateau).

only goal was to confirm that the mirror electrodes are capable of reflecting the ion bunch. The time constant τ of the mirror electrodes can also estimated from this measurements by looking at the length of the plateaus. With $\tau = 0\,\mu\text{s}$, one would expect a plateau as wide as the trigger-pulse, however, the observed ones are 95 µs and 62 µs wide, respectively. Since the mirror electrodes begin at $\Phi_{\text{mirror}} = 200\,\text{V}$ and start loading once the pulse ends, the unloading time can be estimated by:

$$t_{\text{unload}} = 200\,\mu\text{s} - t_p \ , \tag{4.10}$$

where t_{unload} is the unloading time and t_p is the width of the plateau. The resulting unloading times correspond to 105 µs and 138 µs for the first and second mirror electrodes respectively. The unloading process is defined by

$$\Phi(t) = \Phi_{\text{mirror}} e^{t/\tau}. \tag{4.11}$$

Assuming that the plateau starts once the voltages have decreased about 60%, solving Equation 4.11 leads to a time constant τ of 114 µs and 150 µs for each mirror electrode respectively. Now, despite the apparently big time constants, they should not present a big obstacle when re-trapping Ar^{13+} with the elevated ground set to 135 V. This would make an increase of 10 V suffice to reflect the ion bunch and re-trap it in the Paul trap. If Φ_{mirror} is set at 240 V, it would take both electrodes around 15 µs to start reflecting ions. Since the transit time is approximately 40 µs, re-trapping is in the realm of possibility.

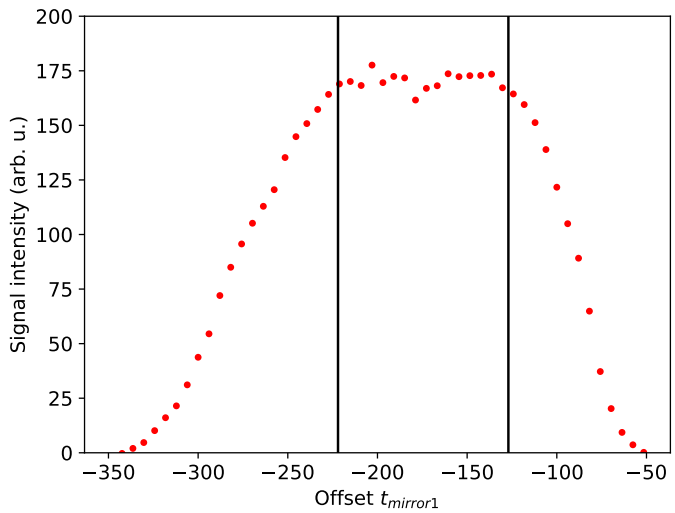

Figure 25: Signal intensity at the MCP behind the Paul trap dependent on the switching time of the mirror electrode before the trap. The start and ending of the plateau are shown in Table 7.

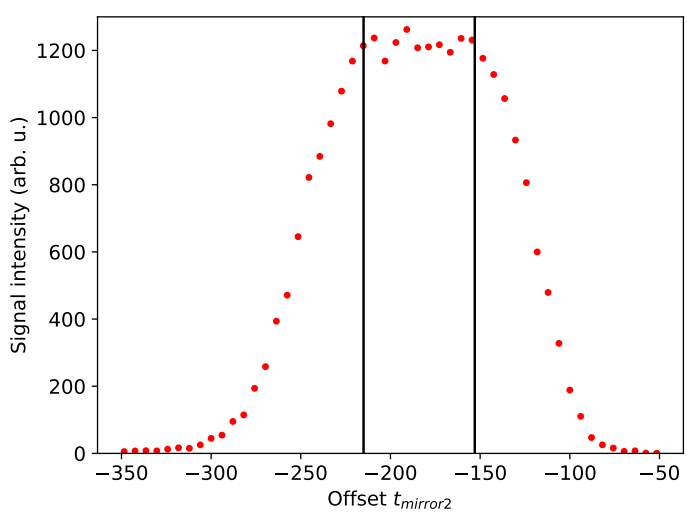

Figure 26: Analog measurement to Figure 25 but with the mirror electrode behind the trap. The black lines depicting the plateau lie at $-215\,\mu s$ and $-153\,\mu s$

.

5 Conclusion and outlook

The optimizations carried in this work present steps towards re-trapping of highly charged argon. Firstly, the desired charge state Ar^{13+} was identified in both MCPs before the trap and then also selected. Figure 21 and Figure 22 are good indicators of the selection of the charge state, since a bad one would have led to the presence of a second peak on the time of flight signal at the MCP and a second line on the spectrum while slowing the ions down. Afterwards, the ions were successfully slowed down to $140\,\mathrm{V} \times$ charge, showing a narrower energy distribution in 24. Finally, the reflection with the mirror electrodes was tested, leading to the conclusion that re-trapping is feasible. The final re-trapping of Ar^{13+} was not carried out yet, due to time constrains.

Nevertheless, both the production and the transport of highly charged argon have been successful and it is reasonable to expect a successful re-trapping in the upcoming weeks or months, proving the concept of the superconducting radio frequency trap.

References

[1] Aldous Huxley. *Brave New World*. New York: Harper Brothers, 1932.

[2] Isaac Newton. "A letter of Mr. Isaac Newton, Professor of the Mathematicks in the University of Cambridge; containing his new theory about light and colors: sent by the author to the publisher from Cambridge, Febr. 6. 1671/72; in order to be communicated to the R. Society". In: *Philosophical Transactions of the Royal Society of London* 6.80 (2014), pp. 3075–3087.

[3] G. Kirchhoff. "Ueber die Fraunhofer'schen Linien". In: *Annalen der Physik* 185.1 (1860), pp. 148–150. DOI: https://doi.org/10.1002/andp.18601850115. eprint: https://onlinelibrary.wiley.com/doi/pdf/10.1002/andp.18601850115. URL: https://onlinelibrary.wiley.com/doi/abs/10.1002/andp.18601850115.

[4] F. Abe et al. "Observation of Top Quark Production in $\overline{p}p$ Collisions with the Collider Detector at Fermilab". In: *Phys. Rev. Lett.* 74 (14 Apr. 1995), pp. 2626–2631. DOI: 10.1103/PhysRevLett.74.2626. URL: https://link.aps.org/doi/10.1103/PhysRevLett.74.2626.

[5] S. Abachi et al. "Observation of the Top Quark". In: *Phys. Rev. Lett.* 74 (14 Apr. 1995), pp. 2632–2637. DOI: 10.1103/PhysRevLett.74.2632. URL: https://link.aps.org/doi/10.1103/PhysRevLett.74.2632.

[6] M. L. Perl et al. "Evidence for Anomalous Lepton Production in e^+-e^- Annihilation". In: *Phys. Rev. Lett.* 35 (22 Dec. 1975), pp. 1489–1492. DOI: 10.1103/PhysRevLett.35.1489. URL: https://link.aps.org/doi/10.1103/PhysRevLett.35.1489.

[7] G. Aad et al. "Observation of a new particle in the search for the Standard Model Higgs boson with the ATLAS detector at the LHC". In: *Physics Letters B* 716.1 (2012), pp. 1–29. ISSN: 0370-2693. DOI: https://doi.org/10.1016/j.physletb.2012.08.020. URL: https://www.sciencedirect.com/science/article/pii/S037026931200857X.

[8] M. G. Kozlov et al. "Highly charged ions: Optical clocks and applications in fundamental physics". In: *Rev. Mod. Phys.* 90 (4 Dec. 2018), p. 045005. DOI: 10.1103/RevModPhys.90.045005. URL: https://link.aps.org/doi/10.1103/RevModPhys.90.045005.

[9] Morton A Levine et al. "The Electron Beam Ion Trap: A New Instrument for Atomic Physics Measurements". In: *Physica Scripta* T22 (Jan. 1988), pp. 157–163. DOI: 10.1088/0031-8949/1988/t22/024. URL: https://doi.org/10.1088/0031-8949/1988/t22/024.

[10] ED Donets. "The Physics and Technology of Ion Sources". In: *Wiley, New York* (1989), p. 245.

[11] P. Micke et al. "The Heidelberg compact electron beam ion traps". In: *Review of Scientific Instruments* 89.6 (2018), p. 063109. DOI: 10.1063/1.5026961. eprint: https://doi.org/10.1063/1.5026961. URL: https://doi.org/10.1063/1.5026961.

[12] Elwin Arthur Dijck. "Spectroscopy of Trapped $^{138}Ba^{+}$ Ions for Atomic Parity Violation and Optical Clocks". PhD thesis. Groningen U., 2020. DOI: 10.33612/diss.108023683.

[13] J. Stark. "An Ultralow-Noise Superconducting Radio-Frequency Ion Trap for Frequency Metrology with Highly Charged Ions". PhD thesis. Ruprecht-Karls-Universität Heidelberg, 2020. DOI: https://doi.org/10.11588/heidok.00028742.

[14] J. Nauta. "An extreme-ultraviolet frequency comb enabling frequency metrology with highly charged ions". PhD thesis. Ruprecht-Karls-Universität Heidelberg, 2020. DOI: http://hdl.handle.net/21.11116/0000-0007-636C-1.

[15] J. Nauta et al. "XUV frequency comb production with an astigmatism-compensated enhancement cavity". In: *Opt. Express* 29.2 (Jan. 2021), pp. 2624–2636. DOI: 10.1364/OE.414987. URL: http://www.opticsexpress.org/abstract.cfm?URI=oe-29-2-2624.

[16] Wolfgang Lotz. "Electron-impact ionization cross-sections and ionization rate coefficients for atoms and ions from hydrogen to calcium". In: *Zeitschrift für Physik* 216 (3), pp. 241–247. DOI: 10.1007/BF01392963. URL: https://doi.org/10.1007/BF01392963.

[17] Young Soon Kim and R. H. Pratt. "Direct radiative recombination of electrons with atomic ions: Cross sections and rate coefficients". In: *Phys. Rev. A* 27 (6 June 1983), pp. 2913–2924. DOI: 10.1103/PhysRevA.27.2913. URL: https://link.aps.org/doi/10.1103/PhysRevA.27.2913.

[18] Vladimir I. Fisher et al. "Electron-impact-excitation cross sections of hydrogenlike ions". In: *Phys. Rev. A* 55 (1 Jan. 1997), pp. 329–334. DOI: 10.1103/PhysRevA.55.329. URL: https://link.aps.org/doi/10.1103/PhysRevA.55.329.

[19] Alfred Müller and Erhard Salzborn. "Scaling of cross sections for multiple electron transfer to highly charged ions colliding with atoms and molecules". In: *Physics Letters A* 62.6 (1977), pp. 391–394. ISSN: 0375-9601. DOI: https://doi.org/10.1016/0375-9601(77)90672-7. URL: https://www.sciencedirect.com/science/article/pii/0375960177906727.

[20] G. Fussmann, C. Biedermann, and R. Radtke. "EBIT: An Electron Beam Source for the Production and Confinement of Highly Ionized Atoms". In: *Advanced Technologies Based on Wave and Beam Generated Plasmas*. Ed. by H. Schlüter and A. Shivarova. Dordrecht: Springer Netherlands, 1999, pp. 429–468. ISBN: 978-94-017-0633-9. DOI: 10.1007/978-94-017-0633-9_19. URL: https://doi.org/10.1007/978-94-017-0633-9_19.

[21] R.E. Marrs. "Self-cooling of highly charged ions during extraction from electron beam ion sources and traps". In: *Nuclear Instruments and Methods in Physics Research Section B: Beam Interactions with Materials and Atoms* 149.1 (1999), pp. 182–194. ISSN: 0168-583X. DOI: https://doi.org/10.1016/S0168-583X(98)00624-7. URL: https://www.sciencedirect.com/science/article/pii/S0168583X98006247.

[22] L. Schmoger. "Ein elektrodynamisches System für den Transfer hochgeladener Ionen in eine Paulfalle". Diploma thesis. Ruprecht-Karls-Universität Heidelberg, 2013. DOI: http://hdl.handle.net/11858/00-001M-0000-000E-EDFE-0.

[23] "Electrostatic Deflection". In: *Applied Charged Particle Optics*. Berlin, Heidelberg: Springer Berlin Heidelberg, 2008, pp. 45–66. ISBN: 978-3-540-71925-0. DOI: 10.1007/978-3-540-71925-0_2. URL: https://doi.org/10.1007/978-3-540-71925-0_2.

[24] L. Schmoeger. "Kalte hochgeladene Ionen für Frequenzmetrologie". PhD thesis. Ruprecht-Karls-Universität Heidelberg, 2017. DOI: http://hdl.handle.net/11858/00-001M-0000-002E-25A5-B.

[25] P. Micke. "Quantum Logic Spectroscopy of Highly Charged Ions". PhD thesis. Gottfried Wilhelm Leibniz Universität Hannover und Physikalisch-Technische Bundesanstalt, Braunschweig, 2020. DOI: https://doi.org/10.7795/110.20201222.

[26] M. K. Rosner. "Production and preparation of highly charged ions for re-trapping in ultra-cold environments". MA thesis. Ruprecht-Karls-Universität Heidelberg, 2019. DOI: http://hdl.handle.net/21.11116/0000-0005-5B37-8.

[27] K. Blaum. *Stored Charged Particles*. Vorlesungsskript. 2020.

[28] John Gillaspy. *Trapping Highly Charged Ions: Fundamentals and Applications*. en. Nova Publisher, Hauppauge, NY, 2000-04-01 2000.

[29] A. Kramida et al. NIST Atomic Spectra Database (ver. 5.8), [Online]. Available: `https://physics.nist.gov/asd` [2021, June 21]. National Institute of Standards and Technology, Gaithersburg, MD. 2020.

Appendix

Ionization energy of argon

Ion species	Ionization energy / eV	Principal quantum number n
Ar	15.759 611 9(5)	3
Ar^{1+}	27.629 67(12)	3
Ar^{2+}	40.735(12)	3
Ar^{3+}	59.58(18)	3
Ar^{4+}	74.84(17)	3
Ar^{5+}	91.290(10)	3
Ar^{6+}	124.41(6)	3
Ar^{7+}	143.4567(12)	3
Ar^{8+}	422.60(6)	2
Ar^{9+}	479.76(12)	2
Ar^{10+}	540.4(6)	2
Ar^{11+}	619.0(4)	2
Ar^{12+}	685.5(3)	2
Ar^{13+}	755.13(22)	2
Ar^{14+}	855.5(3)	2
Ar^{15+}	918.375(7)	2
Ar^{16+}	4123.665 57(4)	1
Ar^{17+}	4423.2229(7)	1

Table 8: Ionization energy of each argon charge state. The change in n is the reason for the big jumps between Ar^{7+} and Ar^{8+} as well as between Ar^{15+} and Ar^{16+}. [29]

Acknowledgements

I would like to thank first and foremost Silvia and Nick for supporting me through all my thesis and for making my live overall easier. Also many thanks to José for taking me in his group and helping me whenever I needed it. This also applies to all the seniors of the group, Julian, Karl, Elwin and Christian, whom I also want to thank for their corrections and mentoring. Last but not least, I'm also thankful for the people at the students' office, who are sort of good people and the Checker group, who are kind of better.

Erklärung

Ich versichere, dass ich diese Arbeit selbstständig verfasst und keine anderen als die angegebenen Quellen und Hilfsmittel benutzt habe.

Heidelberg, den 9. Juni 2021,

Alvaro